OPTIMAL DESIGN OF MULTIPHASE COMPOSITES UNDER ELASTODYNAMIC LOADING

R. TAVAKOLI

Abstract. An algorithm is proposed to optimize the performance of multiphase structures (composites) under elastodynamic loading conditions. The goal is to determine the distribution of material in the structure such that the time-averaged total stored energy of structure is minimized. A penalization strategy is suggested to avoid the checkerboard instability, simultaneously to generate near 0-1 topologies. As a result of this strategy, the solutions of presented algorithm are sufficiently smooth and possess the regularity of H^1 function space. A new way for the adjoint sensitivity analysis of the corresponding PDE-constrained optimization problem is presented. It is general and can be easily applied to a vide range of alternative problems. The success of introduced algorithm is studied by numerical experiments on a two-dimensional model problem for different numbers of phases ranging from 2 to 5. According to numerical results, the objective functional is reduced monotonically with iterations. It is reduced more than an order of magnitude after a few iterations of the presented algorithm. Moreover, the final topologies at the optimal solutions are near 0-1. The dynamic behavior of optimal designs are compared to initial ones to show the impact of optimization on the performance of structures.

Keywords. Adjoint sensitivity analysis; Multimaterial topology optimization; Optimal design; Regularization; Stress waves.

1. Introduction

Many engineering structures experience elastodynamic loading conditions during their lifetime period, results in the propagation of stress waves in the structures. The interaction of structures with stress waves is an important factor that should be taken into account during their design stage. The topology optimization [1] is a standard method to find unknown layout of structures to improve their performances. The topology optimization of structures under static loading conditions has been well studied in the literature c.f. [1, 2]. Regarding to the topology optimization under the dynamic conditions, many of available works have been focused on the optimal design of structures based on the eigenfrequency analysis, for instance to maximize the smallest eigenvalue of structure under free vibration (c.f. [3–21]). In fact, in these works the quasi steady-state conditions were assumed for the stress waves and so the displacement field is computed by solving a Helmholtz-like PDE in the frequency domain. However, under the actual dynamic loading conditions, the interaction of stress waves with the material inhomogeneities and solid boundaries leads to a complex space-time wave pattern in the body. As a result, the assumption of quasi steady-state conditions and the decomposition of stress waves into the pressure and shear components is not sufficiently feasible [22]. A natural solution to cope this limitation is the space-time analysis of elastic waves in structures.

There are a few works on the topology optimization of structures based on the time-domain analysis (c.f. [23]). Using the homogenization method, the two dimensional time-domain topology optimization problem has been considered in [24]. The objective functional, to be minimized, in this work was the time-averaged dynamic compliance of structure in a finite time-windows. The three-dimensional form of this problem has been studied in [22] to find the optimal layout of functionally graded materials. Mono-dimensional topology optimization under transient loading has been considered in [25] for the optimal design of inhomogeneous solids that exhibit desired band-gap structures.

Date: July 12, 2015.

R. Tavakoli, Materials Science and Engineering Department, Sharif University of Technology, Tehran, Iran, P.O. Box 11365-9466, tel: 982166165209, fax: 982166005717, email: rtavakoli@sharif.ir.

The optimal determination of space-time materials layout was considered in [26]. In this work, the dynamics of structure was governed by the one dimensional linear wave equation that includes a damping term. The corresponding objective functional depends on the gradient and time derivative of the displacement field. Later, this problem has been extended to higher dimensions in [27, 27, 28]. A similar problem, however without the damping term has been considered in [29]. The optimization of space-time material layout for the one-dimensional wave propagation problem with varying mass and stiffness parameters has been investigated in [30, 31]. The topology optimization of low contrast two-phase composites subjected to the wave equation has been studied in [32]. By assuming the low contrast between phase, the authors used a second order asymptotic expansion with respect to the small amplitude of the phase coefficients that helps them to rigorously prove the existence of solution for this problem by means of the relaxation theory (c.f. [2]). These authors examined several variants of objective functionals and they supported their theory by several numerical experiments. In [33], it has been experimentally and theoretically shown that the stress-waves in solids can be controlled through imposing graded changes in the material properties. Inspiring from this work, the topology optimization based on the homogenization method has been adapted in [34] for the optimal management of stress waves in solids. In this work, different objective functionals have been introduced to find the optimal layout of a rank-N laminated composite structure for damping, redirecting and focusing of elastic stress waves. The topology optimization of energy dissipating structures under impact loading is studied in [35] for rate-independent elastoplastic materials.

Recently, there has been an increasing interest in solving topology optimization problems using more than two phases [36, 37]. It is particularly attractive for the optimal design of engineering structures under transient loading conditions. An interesting question in this context is that whether increasing the number of contributing phases can improve the dynamic performance of structures. There are several efforts on the multimaterial topology optimization under static loading conditions. For instance, it has been solved by the MMA method [38–41], optimality criteria approach [36], level set method [42–51], phase-field approach [37, 52–57], discrete material optimization method [58–60] and shape function parameterization scheme [61–63].

According to our knowledge, there is no work on the time-domain multimaterial topology optimization under elastodynamic loading conditions. The goal of present study is introduce a numerical method to solve multiphase topology optimization problems under elastodynamics loading conditions. The remainder of this paper is organized as follows. The mathematical formulation of the corresponding topology optimization problem is presented in the next section. According to our numerical experiments, to attain near 0-1 topologies, i.e. having the sufficient contrast between phases, is difficult in practice, because the optimal solutions tend to smear the interfaces between phases. For instance, using the SIMP penalization approach does not lead to satisfactory outcomes. Following [37], the penalization of problem based on the combination of SIMP and phase-field approaches is presented in section 2, to cope the mentioned difficulty. Section 3 presents the first order necessary optimality conditions corresponding to the penalized optimal design problem. A new adjoint sensitivity analysis is presented in this section to compute the first variation of the corresponding objective function. The minimization algorithm based on the regularized projected steepest descent method is presented in section 4. Section 5 briefly mentions the discretization schemes used for the numerical solution of this optimal design problem. Section 6 is devoted to the evaluation of presented algorithm by means of numerical experiments. Finally, section 7 summarizes this paper.

2. Problem Formulation

2.1. **Multimaterial elastodynamic topology optimization problem.** Consider Ω as the design domain that is a fixed nonempty and sufficiently regular subset of $\mathbb{R}^d$ $(d = 1, 2, 3)$. It is assumed that Ω is occupied by $p \in \mathbb{N}$ $(p \geqslant 2)$ number of distinct isotropic linearly elastic materials. The distribution of materials in Ω is determined by their local volume fractions that are denoted by field variables $\phi_i(\boldsymbol{x})$ $(i = 1, \ldots, p)$, where $\phi_i \in \mathcal{V}(\Omega)$ and $\mathcal{V}$ denotes a sufficiently regular function space. Whenever it is beneficial, these field variables are denoted by the vector field Φ for the purpose of brevity, i.e. $\Phi = (\phi_1, \ldots, \phi_p)^T$. Assume that the displacement vector in Ω is denoted by the vector

filed $\boldsymbol{u} \in \mathcal{U}(\Omega)$, where $\mathcal{U}$ is a sufficiently regular function space. For a given materials distribution Φ, the dynamics of $\boldsymbol{u}$ is governed by the following partial differential equation (PDE):

$$\left\{\begin{array}{rcll} \rho\ \ddot{\boldsymbol{u}} & = & \nabla\cdot(\boldsymbol{C}:\mathcal{D}(\boldsymbol{u}))+\boldsymbol{f} & \texttt{in}\quad \Omega\times(0,T] \\ (\boldsymbol{C}:\mathcal{D}(\boldsymbol{u}))\cdot\boldsymbol{n} & = & \hat{\boldsymbol{t}}(\boldsymbol{x},t) & \texttt{on}\quad \Gamma_t\times(0,T] \\ \boldsymbol{u}(\boldsymbol{x},t) & = & \hat{\boldsymbol{u}}(\boldsymbol{x},t) & \texttt{on}\quad \Gamma_u\times(0,T] \\ \boldsymbol{u}(\boldsymbol{x},0) & = & \boldsymbol{u}_0(\boldsymbol{x}) & \texttt{in}\quad \Omega\times\{t=0\} \\ \dot{\boldsymbol{u}}(\boldsymbol{x},0) & = & \dot{\boldsymbol{u}}_0(\boldsymbol{x}) & \texttt{in}\quad \Omega\times\{t=0\} \end{array}\right. \tag{1}$$

where $[0,T]$ denotes the temporal domain, $\hat{\boldsymbol{t}}$ denotes the traction of structure with the environment through traction boundaries, Γ_t, $\hat{\boldsymbol{u}}$ denotes the prescribed displacement on boundaries Γ_u, $\partial\Omega = \Gamma_t\cup\Gamma_u$, $\boldsymbol{u}_0$ denotes the initial displacement field, $\dot{\boldsymbol{u}}_0$ denotes the initial velocity field and $\boldsymbol{f}=\boldsymbol{f}(\boldsymbol{x})$ denotes the volumetric body force inside Ω. Moreover, $\mathcal{D}(\boldsymbol{u}) := \frac{1}{2}(\nabla\boldsymbol{u}+(\nabla\boldsymbol{u})^T) = \frac{1}{2}(\partial_i u_j + \partial_j u_i)_{i,j},\ i,j=1\ldots,d$. Note that the double dot operator, :, denotes the usual contraction over two sets of indices. Furthermore, $\rho=\rho(\Phi(\boldsymbol{x}))$ denotes the density and $\boldsymbol{C}=\boldsymbol{C}(\Phi(\boldsymbol{x}))$ denotes the elasticity tensor which is a forth order supersymmetric tensor (symmetric in both the right and the left Cartesian index pair, together with symmetry under the interchange of the pairs).

Following [36, 37, 55], the SIMP approach is used for the purpose materials interpolation in the present study. Therefore, for the elasticity tensor we have:

$$\boldsymbol{C}(\Phi)=\sum_{i=1}^{p}\phi_i^q\ \boldsymbol{C}_i \tag{2}$$

where $q\geqslant 1$ is the SIMP penalization power and $\boldsymbol{C}_i$ is the constant stiffness tensor corresponding to the i-th phase. The main benefits of using the SIMP-based interpolation are its simplicity, ease of extension to arbitrary number of phases and its practical satisfactory results. For these reasons, it has been extensively used in the literature of multimaterial topology optimization, see for instance [36, 37, 54, 55, 60, 64–66]. It is however important to note that the interpolation of $\boldsymbol{C}$ based on (2) does not always leads to feasible results. It can result in nonphysical data. For instance, the elasticity tensor may violate the Hashin-Shtrikman bounds [1]. According to [1, 22, 67], a reasonable interpolation scheme is to compute the effective properties by averaging between the HashinShtrikman upper and lower bounds. However, it is not easy to find the explicit form of Hashin-Shtrikman bounds for $p>3$. Moreover, Hashin-Shtrikman bounds are attainable under certain conditions on the volume fractions and physical properties of contributing materials [41]. On the other hand, if the optimization algorithm results in a near 0-1 topology, by virtue, the materials interpolation scheme (2) does not effect on the validity of final solution. However, it may change the intermediate optimization path. In the present study we are going to develop a computational algorithm that results in near 0-1 topologies. Therefore, the materials interpolation based on (2) will be used in this work.

Similar to (2), the local density is computed by the SIMP approach in this study:

$$\rho(\Phi)=\sum_{i=1}^{p}\phi_i^q\ \rho_i \tag{3}$$

where ρ_i denotes the density of i-th phase.

The time-averaged total stored energy in Ω in time interval $[0,T]$ is considered as the objective functional, $\mathcal{J}$, in the present study:

$$\mathcal{J}(\Phi,\boldsymbol{u})=\frac{1}{2}\int_0^T\int_\Omega\Big(\rho\ \dot{\boldsymbol{u}}^2+\big(\boldsymbol{C}:\mathcal{D}(\boldsymbol{u})\big):\mathcal{D}(\boldsymbol{u})\Big)\,d\boldsymbol{x}\,dt \tag{4}$$

In addition to equation (1), our optimization problem has several constraints on the design vector Φ that are mentioned as follows. Obviously, we have the following pointwise bound constraints on every ϕ_i,

$$0\leqslant\phi_i\leqslant 1,\quad i=1,\ldots,p \tag{5}$$

Since no overlap and gap between materials are allowed in our formulation, the summation of volume fractions at every point $\boldsymbol{x} \in \Omega$ should be equal to unity:

$$\sum_{i=1}^{p} \phi_i = 1 \tag{6}$$

where the summation operator is to be understood componentwise, local, here. The intersection of (5) and (6) is commonly called the Gibbs simplex in the materials science literature. Furthermore, we consider the p number of global volume constraints on the total volume fractions of materials in Ω:

$$\int_{\Omega} \phi_i \; d\boldsymbol{x} = \Lambda_i |\Omega|, \quad i = 1, \dots, p \tag{7}$$

where Λ_i denotes the total volume fraction of phase i in Ω. Obviously we have $0 \leqslant \Lambda_i \leqslant 1$ and $\sum_{i=1}^{p} \Lambda_i = 1$. Therefore, the admissible design space, denoted by $\mathcal{A}$ here, can be stated as follows:

$$\mathcal{A} := \left\{ \Phi \in \mathcal{V}^p(\Omega) \;\middle|\; \begin{array}{ll} \sum_{i=1}^{p} \phi_i = 1, & \\ \int_{\Omega} \phi_i \; d\boldsymbol{x} = \Lambda_i |\Omega|, & i = 1, \dots, p \\ 0 \leqslant \phi_i \leqslant 1, & i = 1, \dots, p \end{array} \right\}$$

The constraint qualification is a common requirement for the success of optimization algorithms from both the theoretical and practical points of views [37, 68]. To obtain the qualification of constraints for linearly constrained optimization problems, it is sufficient to show that the equality constraints are linearly independent and that there exists a feasible point satisfying all inequalities strictly (c.f. [69]). However as it is discussed in [37, 70], the set of equality constraints in $\mathcal{A}$ are not linearly independent. Assuming that $\mathcal{A}$ is nonempty, to ensure the qualification of constraint, we remove ϕ_p from the set of unknowns using (6), i.e. $\phi_p = 1 - \sum_{i=1}^{p-1} \phi_i$. Therefore, we redefine the admissible design space $\mathcal{A}$ as follows:

$$\mathcal{A} \overset{\texttt{redefine}}{:=} \left\{ \Phi \in \mathcal{V}^{p-1}(\Omega) \;\middle|\; \begin{array}{ll} \int_{\Omega} \phi_i \; d\mathbf{x} = \Lambda_i |\Omega|, & i = 1, \dots, p-1 \\ 0 \leqslant \phi_i \leqslant 1, & i = 1, \dots, p-1 \\ 0 \leqslant \sum_{i=1}^{p-1} \phi_i \leqslant 1, & \end{array} \right\}$$

where the design vector Φ is redefined as $\Phi = (\phi_1, \dots \phi_{p-1})^T$. Because all constraints in $\mathcal{A}$ are linear, $\mathcal{A}$ is convex set. In the remainder of this work, we will use symbol Φ to denote both of vector fields $(\phi_1, \dots \phi_p)^T$ and $(\phi_1, \dots \phi_{p-1})^T$ wherever it is applicable.

Putting all together, we are going to solve the following optimization problem:

$$\min_{(\Phi,\, \boldsymbol{u}) \,\in\, (\mathcal{A},\, \mathcal{U})} \mathcal{J}\big(\Phi, \boldsymbol{u}(\Phi)\big) \quad \texttt{subject to : equation (1)} \tag{8}$$

2.2. **Regularization by Perimeter Penalization.** Mesh dependency, topological instability and checkerboard patterns [71] are of the famous difficulties during the numerical solution of topology optimization problems. The density filtering, sensitivity filtering and perimeter penalization are commonly used to overcome these problems [71]. The penalization of objective functional with the interphase perimeter has been firstly used in [72] to avoid the topological instability during the binary-phase topology optimization problem. Later, this method has been extensively used in the literature to solve topology optimization problems, for instance see [66, 73–77].

Following [37], the approximation of the total interphase perimeter based on the extended Modica and Mortola [78–81] approach is used in this work to regularize the original optimization problem. For this purpose, the objective functional is penalized by the following functional:

$$P^{\varepsilon}(\Phi) = \sum_{i=1}^{p-1} \int_{\Omega} \frac{\varepsilon}{2} \; |\nabla \phi_i|^2 \; d\boldsymbol{x} + \sum_{i=1}^{p-1} \int_{\Omega} \frac{1}{\varepsilon} \; W(\phi_i) \; d\boldsymbol{x} \tag{9}$$

where $\varepsilon \in \mathbb{R}^+$ is the regularization parameter and W denotes the symmetric double-well function that assumes its minimizers at 0, 1 and $W(0) = W(1) = 0$. This function can be defined as follows:

$$W(r) = r^2 (1 - r)^2 \tag{10}$$

According to [81], P^{ε} Γ-converges to the total perimeter between boundaries of phases as $\varepsilon \to 0$.

The regularized form of optimization problem (8) can be expressed as follows,

$$\min_{(\Phi,\ \boldsymbol{u})\ \in\ (\mathcal{A},\ \mathcal{U})} \mathcal{J}^{\varepsilon,\zeta}\big(\Phi,\mathbf{u}(\Phi)\big) \quad \texttt{subject to}: \quad \texttt{equation}\ (1) \tag{11}$$

where $\zeta > 0$ denotes the penalization parameter and,

$$\mathcal{J}^{\varepsilon,\zeta}\big(\Phi,\mathbf{u}(\Phi)\big) := \mathcal{J}\big(\Phi,\mathbf{u}(\Phi)\big) + \zeta P^{\varepsilon}(\Phi)$$

3. Optimality conditions

The first order necessary optimality conditions for problem (11) will be presented in this section. Following [37, 70, 82], we shall express optimality conditions based on the projected gradient approach.

3.1. Optimality conditions based on the projected gradient approach.

Lets to briefly recall the results of propositions 2.4 and 2.5 of [70] here, that are used in this section to derive the first order necessary optimality conditions for problem (11).

Proposition 3.1. *(the necessary optimality conditions based on the projected gradient and its descent property [70]) Let $\mathcal{W}$ be a Hilbert space and $\mathcal{K}$ as a convex closed nonempty subset of $\mathcal{W}$. Assume the functional $J(w) : \mathcal{K} \to \mathbb{R}$ is differentiable at $w \in \mathcal{K}$ with the directional derivative denoted by $J'(w)$. If w^* denotes a local minimizer of $J(w)$ over $\mathcal{K}$, then:*

$$J'_{\mathcal{K}}(w^*) := \mathscr{P}_{\mathcal{K}}[w^* - J'] - w^* = 0 \quad \texttt{a.e.} \tag{12}$$

Since $\mathscr{P}_{\mathcal{K}}[w - J'] - w$ is equal to the projected gradient of J at w (c.f. [83]), the constrained stationary points of J are roots of the projected gradient with respect to set $\mathcal{K}$. Therefore we call (12) *the necessary optimality conditions based on the projected gradient method. Moreover, we have:*

$$\langle J'(w),\ J'_{\mathcal{K}}(w)\rangle \leqslant -\|J'_{\mathcal{K}}(w)\|^2 \tag{13}$$

Therefore, (12) *and* (13) *suggest the following iterative procedure for the constrained minimization of $J(w)$:*

$$w_{k+1} = w_k + \alpha_k J'_{\mathcal{K}}(w_k), \quad k = 0, 1, \ldots, \tag{14}$$

where subscript k denotes the iterations counter, w_0 denotes the initial guess and $\alpha_k \in (0, 1]$ is computed based on an appropriate globalization strategy (cf. [69]).

3.2. First order adjoint sensitivity analysis.

Similar to [37, 70], in the present study, we mange the control constraints (set $\mathcal{A}$) by the projected gradient method and use the projected steepest descent algorithm (c.f. equation (14)) to minimize $\mathcal{J}^{\varepsilon,\zeta}$. Therefore, we ignore control constraints in this subsection for the sake of convenience. To use the projected steepest descent algorithm, it is required to compute the gradient of objective functional $\mathcal{J}^{\varepsilon,\zeta}$ with respect to the design vector Φ considering the PDE constraint (1). This procedure is commonly called the adjoint sensitivity analysis in the computational engineering literature (cf. [1, 84, 85]).

The directional derivative (first variation) of the objective functional $\mathcal{J}^{\varepsilon,\zeta}$ with respect to Φ, denoted by $\mathcal{J}' = (\mathcal{J}'_1, \ldots, \mathcal{J}'_{p-1})^T$, is computed by means of the adjoint approach in this subsection. Our derivation here is closely related to the classical derivation of first order necessary optimality conditions based on KKT conditions (cf. [69, 86, 87]). Unlike former methods, there is no heuristic or specific treatment in our derivation such that the adjoint PDE and its corresponding initial and boundary conditions are directly resulted from our analysis. Moreover, this method can be straightforwardly extended to different classes of PDE constrained optimization problems.

Consider sufficiently regular (adjoint) functions $\boldsymbol{v}$, $\boldsymbol{v}_s$ and $\boldsymbol{v}_v$ defined in $\Omega \times (0, T]$, $\Omega \times \{t = 0\}$ and $\Omega \times \{t = 0\}$ respectively. Furthermore, consider functions $\boldsymbol{v}_t$ and $\boldsymbol{v}_u$ defined on boundaries $\Gamma_t \times (0, T]$ and $\Gamma_t \times (0, T]$ respectively. Ignoring the control constraints, the augmented lagrangian

corresponding to the optimization problem (11) can be expressed as follows:

$$\begin{aligned}\mathcal{L}(\Phi,\boldsymbol{u},\boldsymbol{v},\boldsymbol{v}_t,\boldsymbol{v}_u,\boldsymbol{v}_s,\boldsymbol{v}_v) = &\frac{1}{2}\int_0^T\int_\Omega \Big(\rho\ \dot{\boldsymbol{u}}^2 + \big(\boldsymbol{C}:\mathcal{D}(\boldsymbol{u})\big):\mathcal{D}(\boldsymbol{u})\Big)\ d\boldsymbol{x}\ dt\\ &+\int_0^T\int_\Omega \boldsymbol{v}\cdot\Big(\rho\ \ddot{\boldsymbol{u}} - \nabla\cdot\big(\boldsymbol{C}:\mathcal{D}(\boldsymbol{u})\big)\Big)\ d\boldsymbol{x}\ dt\\ &+\int_0^T\int_{\Gamma_t} \boldsymbol{v}_t\cdot\Big(\big(\boldsymbol{C}:\mathcal{D}(\boldsymbol{u})\big)\cdot\boldsymbol{n} - \hat{\boldsymbol{t}}(\boldsymbol{x},t)\Big)\ d\boldsymbol{x}\ dt\\ &+\int_0^T\int_{\Gamma_u} \boldsymbol{v}_u\cdot\big(\boldsymbol{u}(\boldsymbol{x},t) - \hat{\boldsymbol{u}}(\boldsymbol{x},t)\big)\ d\boldsymbol{x}\ dt\\ &+\int_\Omega \boldsymbol{v}_s\cdot\big(\boldsymbol{u}(\boldsymbol{x},0) - \boldsymbol{u}_0(\boldsymbol{x})\big)\ d\boldsymbol{x}\\ &+\int_\Omega \boldsymbol{v}_v\cdot\big(\dot{\boldsymbol{u}}(\boldsymbol{x},0) - \dot{\boldsymbol{u}}_0(\boldsymbol{x})\big)\ d\boldsymbol{x}\\ &+\zeta\sum_{j=1}^{p-1}\int_\Omega\left(\frac{\varepsilon}{2}\ |\nabla\phi_j|^2 + \frac{1}{\varepsilon}\ W(\phi_j)\right)\ d\boldsymbol{x}\end{aligned} \tag{15}$$

Note that introducing the lagrange multipliers corresponding to the boundary and initial conditions, and direct augmentation of these constraints into $\mathcal{L}$ is not a common way in the engineering literature. However, it is an easy and sound way to rigourously drive the adjoint PDE and its corresponding initial and boundary conditions. This treatment will be well understood by considering the derivation of necessary optimality conditions based on the KKT optimality conditions (cf. [86, 87]).

Assume that the set of points that satisfy the necessary optimality conditions corresponding to problem (11) is denoted by $\mathcal{S}$. Obviously, the local solutions of (11) are members of $\mathcal{S}$. Ignoring the control constraints, $\mathcal{S}$ is in fact equivalent to the set of stationary points of lagrangian $\mathcal{L}$. Therefore, it is sufficient to compute the directional derivative of $\mathcal{L}$ with respect to its input arguments and to equate them to zeros (cf. chapter 10 of [85]). The directional derivatives of $\mathcal{L}$ with respect to functions $\boldsymbol{v}$, $\boldsymbol{v}_t$, $\boldsymbol{v}_u$, $\boldsymbol{v}_s$ and $\boldsymbol{v}_v$ and equating them to zeros results in the direct PDE (1). The directional derivatives of $\mathcal{L}$ with respect to Φ results in:

$$\begin{aligned}\mathcal{L}_{\phi_i}(\Phi,\boldsymbol{u},\boldsymbol{v},\boldsymbol{v}_t,\boldsymbol{v}_u,\boldsymbol{v}_s,\boldsymbol{v}_v)(\delta\phi_i) = &\frac{1}{2}\int_0^T\int_\Omega \Big(\rho_{\phi_i}\ \dot{\boldsymbol{u}}^2 + \big(\boldsymbol{C}_{\phi_i}:\mathcal{D}(\boldsymbol{u})\big):\mathcal{D}(\boldsymbol{u})\Big)\ \delta\phi_i\ d\boldsymbol{x}\ dt\\ &+\int_0^T\int_\Omega \rho_{\phi_i}\boldsymbol{v}\cdot\ddot{\boldsymbol{u}}\ \delta\phi_i\ d\boldsymbol{x}\ dt\\ &-\int_0^T\int_\Omega \boldsymbol{v}\cdot\Big(\nabla\cdot\big(\boldsymbol{C}_{\phi_i}\delta\phi_i:\mathcal{D}(\boldsymbol{u})\big)\Big)\ d\boldsymbol{x}\ dt\\ &+\int_0^T\int_{\Gamma_t} \boldsymbol{v}_t\cdot\big(\boldsymbol{C}_{\phi_i}:\mathcal{D}(\boldsymbol{u})\big)\cdot\boldsymbol{n}\ \delta\phi_i\ d\boldsymbol{x}\ dt\\ &+\zeta\varepsilon\int_\Omega \nabla\phi_i\cdot\nabla\delta\phi_i\ d\boldsymbol{x} + \frac{\zeta}{\varepsilon}\int_\Omega W'(\phi_i)\ \delta\phi_i\ d\boldsymbol{x}\\ &:= \mathtt{I_1}+\mathtt{I_2}-\mathtt{I_3}+\mathtt{I_4}+\mathtt{I_5}+\mathtt{I_6}=0\end{aligned} \tag{16}$$

for $i=1,\dots,p-1$, where the subscript ϕ_i denotes partial differentiation with respect to ϕ_i, i.e. $(\cdot)_{\phi_i}=\partial(\cdot)/\partial\phi_i$, $W'(r)=4r^3-6r^2+2r$. Considering constraint $\phi_p=1-\sum_{i=1}^{p-1}\phi_i$, the differentiation of (2) and (3) with respect to ϕ_i results in:

$$\boldsymbol{C}_{\phi_i}(\Phi) = q\big(\phi_i^{q-1}\boldsymbol{C}_i - \phi_p^{q-1}\boldsymbol{C}_p\big),\quad \texttt{for}\ \ \mathtt{i}=1,\dots,\mathtt{p}-1 \tag{17}$$

$$\rho_{\phi_i}(\Phi) = q\big(\phi_i^{q-1}\rho_i - \phi_p^{q-1}\rho_p\big),\quad \texttt{for}\ \ \mathtt{i}=1,\dots,\mathtt{p}-1 \tag{18}$$

Using the divergence theorem, $\mathtt{I}_3$ and $\mathtt{I}_5$ can be simplified to the following forms:

$$\begin{aligned}\mathtt{I}_3 = &\int_0^T \int_{\Gamma_t} \boldsymbol{v} \cdot \big(\boldsymbol{C}_{\phi_i} : \mathcal{D}(\boldsymbol{u})\big) \cdot \boldsymbol{n}\ \delta\phi_i\ d\boldsymbol{x}\ dt + \int_0^T \int_{\Gamma_u} \boldsymbol{v} \cdot \big(\boldsymbol{C}_{\phi_i} : \mathcal{D}(\boldsymbol{u})\big) \cdot \boldsymbol{n}\ \delta\phi_i\ d\boldsymbol{x}\ dt \\ &- \int_0^T \int_\Omega \nabla \boldsymbol{v} : \boldsymbol{C}_{\phi_i} : \mathcal{D}(\boldsymbol{u})\ \delta\phi_i\ d\boldsymbol{x}\ dt := \mathtt{I}_{3,1} + \mathtt{I}_{3,2} - \mathtt{I}_{3,3}\end{aligned} \tag{19}$$

$$\mathtt{I}_5 = -\zeta\varepsilon \int_\Omega \Delta\phi_i\ \delta\phi_i\ d\boldsymbol{x} + \zeta\varepsilon \int_\Gamma \nabla\phi_i(\boldsymbol{x}) \cdot \boldsymbol{n}(\boldsymbol{x})\ \delta\phi_i\ d\boldsymbol{x} := -\mathtt{I}_{5,1} + \mathtt{I}_{5,2} \tag{20}$$

where Δ in (20) denotes the classical Laplacian operator, i.e. $\Delta(\cdot) := \nabla \cdot \big(\nabla(\cdot)\big)$. The directional derivatives of $\mathcal{L}$ with respect to $\boldsymbol{u}$ results in:

$$\begin{aligned}\mathcal{L}_{\boldsymbol{u}}(\Phi, \boldsymbol{u}, \boldsymbol{v}, \boldsymbol{v}_t, \boldsymbol{v}_u, \boldsymbol{v}_s, \boldsymbol{v}_v)(\delta\boldsymbol{u}) = &\int_0^T \int_\Omega \rho\ \dot{\boldsymbol{u}} \cdot \delta\dot{\boldsymbol{u}}\ d\boldsymbol{x}\ dt \\ &+ \frac{1}{2}\int_0^T \int_\Omega \Big(\big(\boldsymbol{C} : \mathcal{D}(\delta\boldsymbol{u})\big) : \mathcal{D}(\boldsymbol{u}) + \big(\boldsymbol{C} : \mathcal{D}(\boldsymbol{u})\big) : \mathcal{D}(\delta\boldsymbol{u})\Big)\ d\boldsymbol{x}\ dt \\ &+ \int_0^T \int_\Omega \rho\ \boldsymbol{v} \cdot \delta\ddot{\boldsymbol{u}}\ d\boldsymbol{x}\ dt - \int_0^T \int_\Omega \boldsymbol{v} \cdot \Big(\nabla \cdot \big(\boldsymbol{C} : \mathcal{D}(\delta\boldsymbol{u})\big)\Big)\ d\boldsymbol{x}\ dt \\ &+ \int_0^T \int_{\Gamma_t} \boldsymbol{v}_t \cdot \Big(\big(\boldsymbol{C} : \mathcal{D}(\delta\boldsymbol{u})\big) \cdot \boldsymbol{n}\Big)\ d\boldsymbol{x}\ dt + \int_0^T \int_{\Gamma_u} \boldsymbol{v}_u \cdot \delta\boldsymbol{u}(\boldsymbol{x}, t)\ d\boldsymbol{x}\ dt \\ &+ \int_\Omega \boldsymbol{v}_s \cdot \delta\boldsymbol{u}(\boldsymbol{x}, 0)\ d\boldsymbol{x} + \int_\Omega \boldsymbol{v}_v \cdot \delta\dot{\boldsymbol{u}}(\boldsymbol{x}, 0)\ d\boldsymbol{x} \\ &:= \mathtt{J}_1 + \mathtt{J}_2 + \mathtt{J}_3 - \mathtt{J}_4 + \mathtt{J}_5 + \mathtt{J}_6 + \mathtt{J}_7 + \mathtt{J}_8 = 0\end{aligned} \tag{21}$$

Using the integration by part simplifies $\mathtt{J}_1$ to the following from:

$$\begin{aligned}\mathtt{J}_1 = &\int_\Omega \rho\ \dot{\boldsymbol{u}}(\boldsymbol{x}, T) \cdot \delta\boldsymbol{u}(\boldsymbol{x}, T)\ d\boldsymbol{x} - \int_\Omega \rho\ \dot{\boldsymbol{u}}(\boldsymbol{x}, 0) \cdot \delta\boldsymbol{u}(\boldsymbol{x}, 0)\ d\boldsymbol{x} \\ &- \int_0^T \int_\Omega \rho\ \ddot{\boldsymbol{u}} \cdot \delta\boldsymbol{u}\ d\boldsymbol{x}\ dt := \mathtt{J}_{1,1} - \mathtt{J}_{1,2} - \mathtt{J}_{1,3}\end{aligned} \tag{22}$$

Considering the symmetry of tensor $\boldsymbol{C}$ results in:

$$\mathtt{J}_2 = \int_0^T \int_\Omega \big(\boldsymbol{C} : \mathcal{D}(\boldsymbol{u})\big) : \mathcal{D}(\delta\boldsymbol{u})\ d\boldsymbol{x}\ dt$$

Before continuing the derivation, it is worth to mention a useful identity. For a symmetric tensor $\boldsymbol{A}$ and an arbitrary tensor $\boldsymbol{B}$ the following identity holds:

$$\boldsymbol{A} : \boldsymbol{B} = \boldsymbol{A} : \boldsymbol{B}^T = \frac{1}{2}\ \boldsymbol{A} : (\boldsymbol{B} + \boldsymbol{B}^T) \tag{23}$$

The proof of (23) is simple by using the elementary tensor algebra. Using the divergence theorem and identity (23) simplifies $\mathtt{J}_2$ as follows:

$$\begin{aligned}\mathtt{J}_2 = &\int_0^T \int_{\Gamma_t} \Big(\big(\boldsymbol{C} : \mathcal{D}(\boldsymbol{u})\big) \cdot \boldsymbol{n}\Big) \cdot \delta\boldsymbol{u}\ d\boldsymbol{x}\ dt + \int_0^T \int_{\Gamma_u} \Big(\big(\boldsymbol{C} : \mathcal{D}(\boldsymbol{u})\big) \cdot \boldsymbol{n}\Big) \cdot \delta\boldsymbol{u}\ d\boldsymbol{x}\ dt \\ &- \int_0^T \int_\Omega \Big(\nabla \cdot \big(\big(\boldsymbol{C} : \mathcal{D}(\boldsymbol{u})\big)\big)\Big) \cdot \delta\boldsymbol{u}\ d\boldsymbol{x}\ dt := \mathtt{J}_{2,1} + \mathtt{J}_{2,2} - \mathtt{J}_{2,3}\end{aligned} \tag{24}$$

Applying the integration by part on term $\mathtt{J}_3$ gives:

$$\begin{aligned}\mathtt{J}_3 = &\int_\Omega \rho\ \boldsymbol{v}(\boldsymbol{x},T)\cdot\delta\dot{\boldsymbol{u}}(\boldsymbol{x},T)\ d\boldsymbol{x} - \int_\Omega \rho\ \boldsymbol{v}(\boldsymbol{x},0)\cdot\delta\dot{\boldsymbol{u}}(\boldsymbol{x},0)\ d\boldsymbol{x}\\ &- \int_\Omega \rho\ \dot{\boldsymbol{v}}(\boldsymbol{x},T)\cdot\delta\boldsymbol{u}(\boldsymbol{x},T)\ d\boldsymbol{x} + \int_\Omega \rho\ \dot{\boldsymbol{v}}(\boldsymbol{x},0)\cdot\delta\boldsymbol{u}(\boldsymbol{x},0)\ d\boldsymbol{x}\\ &+ \int_0^T\int_\Omega \rho\ \ddot{\boldsymbol{v}}\cdot\delta\boldsymbol{u}\ d\boldsymbol{x}\ dt := \mathtt{J}_{3,1} - \mathtt{J}_{3,2} - \mathtt{J}_{3,3} + \mathtt{J}_{3,4} + \mathtt{J}_{3,5}\end{aligned} \tag{25}$$

Applying the divergence theorem on term $\mathtt{J}_4$ and considering identity (23) results in:

$$\begin{aligned}\mathtt{J}_4 = &\int_0^T\int_{\Gamma_t} \boldsymbol{v}\cdot\Big(\big(\boldsymbol{C}:\mathcal{D}(\delta\boldsymbol{u})\big)\cdot\boldsymbol{n}\Big)\ d\boldsymbol{x}\ dt + \int_0^T\int_{\Gamma_u} \boldsymbol{v}\cdot\Big(\big(\boldsymbol{C}:\mathcal{D}(\delta\boldsymbol{u})\big)\cdot\boldsymbol{n}\Big)\ d\boldsymbol{x}\ dt +\\ &- \int_0^T\int_{\Gamma_t} \Big(\big(\boldsymbol{C}:\mathcal{D}(\boldsymbol{v})\big)\cdot\boldsymbol{n}\Big)\cdot\delta\boldsymbol{u}\ d\boldsymbol{x}\ dt - \int_0^T\int_{\Gamma_u} \Big(\big(\boldsymbol{C}:\mathcal{D}(\boldsymbol{v})\big)\cdot\boldsymbol{n}\Big)\cdot\delta\boldsymbol{u}\ d\boldsymbol{x}\ dt\\ &+ \int_0^T\int_\Omega \Big(\nabla\cdot\big(\boldsymbol{C}:\mathcal{D}(\boldsymbol{v})\big)\Big)\cdot\delta\boldsymbol{u}\ d\boldsymbol{x}\ dt := \mathtt{J}_{4,1} + \mathtt{J}_{4,2} - \mathtt{J}_{4,3} - \mathtt{J}_{4,4} + \mathtt{J}_{4,5}\end{aligned} \tag{26}$$

The collection of all terms in $\mathcal{L}_{\boldsymbol{u}}$ results in the following abstract form:

$$\begin{aligned}\mathcal{L}_{\boldsymbol{u}}\delta\boldsymbol{u} = &\underbrace{(\mathtt{J}_{3,5} - \mathtt{J}_{4,5} - \mathtt{J}_{1,3} - \mathtt{J}_{2,3})}_{\texttt{in } \Omega\times(0,T]} + \underbrace{(\mathtt{J}_5 + \mathtt{J}_{2,1} - \mathtt{J}_{4,1} + \mathtt{J}_{4,3})}_{\texttt{on } \Gamma_t\times(0,T]} + \underbrace{(\mathtt{J}_6 + \mathtt{J}_{2,2} - \mathtt{J}_{4,2} + \mathtt{J}_{4,4})}_{\texttt{on } \Gamma_u\times(0,T]}\\ &+ \underbrace{(\mathtt{J}_7 + \mathtt{J}_8 - \mathtt{J}_{1,2} - \mathtt{J}_{3,2} + \mathtt{J}_{3,4})}_{\texttt{in } \Omega\times\{t=0\}} + \underbrace{(\mathtt{J}_{1,1} + \mathtt{J}_{3,1} - \mathtt{J}_{3,3})}_{\texttt{in } \Omega\times\{t=T\}} = 0\end{aligned} \tag{27}$$

Note that the terms inside each parenthesis of (27) are defined on the same spatiotemporal domain. Taking $\boldsymbol{v}_t = \boldsymbol{v}$ on boundary Γ_t results in $\mathtt{J}_5 = \mathtt{J}_{4,1}$. Therefore, $\mathtt{J}_5$ cancels $\mathtt{J}_{4,1}$ in the second parenthesis in (27). Since the Dirichlet boundary condition on Γ_u is independent to $\boldsymbol{u}$, $\delta\boldsymbol{u} = 0$ on Γ_u. Therefore, $\mathtt{J}_6 = \mathtt{J}_{2,2} = \mathtt{J}_{4,4} = 0$. Taking $\boldsymbol{v} = 0$ on Γ_u results in $\mathtt{J}_{4,2} = 0$. Because the initial conditions are independent to $\boldsymbol{u}$, $\delta\boldsymbol{u}(\boldsymbol{x},0) = \delta\dot{\boldsymbol{u}}(\boldsymbol{x},0) = 0$. Therefore, $\mathtt{J}_7 = \mathtt{J}_8 = \mathtt{J}_{1,2} = \mathtt{J}_{3,2} = \mathtt{J}_{3,4} = 0$. Taking $\boldsymbol{v}(\boldsymbol{x},T) = 0$, results in $\mathtt{J}_{3,1} = 0$. Putting it altogether, equating $\mathcal{L}_{\boldsymbol{u}}$ to zero leads to the following adjoint PDE:

$$\left\{\begin{array}{rcll} \rho\ \ddot{\boldsymbol{v}} - \nabla\cdot\big(\boldsymbol{C}:\mathcal{D}(\boldsymbol{v})\big) &=& \rho\ \ddot{\boldsymbol{u}} + \nabla\cdot\big(\boldsymbol{C}:\mathcal{D}(\boldsymbol{u})\big) & \texttt{in}\quad \Omega\times(T,0]\\ -\big(\boldsymbol{C}:\mathcal{D}(\boldsymbol{v})\big)\cdot\boldsymbol{n} &=& \big(\boldsymbol{C}:\mathcal{D}(\boldsymbol{u})\big)\cdot\boldsymbol{n} & \texttt{on}\quad \Gamma_t\times(T,0]\\ \boldsymbol{v}(\boldsymbol{x},t) &=& 0 & \texttt{on}\quad \Gamma_u\times(T,0]\\ \boldsymbol{v}(\boldsymbol{x},T) &=& 0 & \texttt{in}\quad \Omega\times\{t=T\}\\ \dot{\boldsymbol{v}}(\boldsymbol{x},T) &=& \dot{\boldsymbol{u}}(\boldsymbol{x},T) & \texttt{in}\quad \Omega\times\{t=T\}\end{array}\right. \tag{28}$$

Note that the initial conditions are available at $t = T$ for the adjoint PDE. Therefore, the adjoint PDE should be integrated in reverse time direction, i.e. within interval $(T, 0]$.

The collection of all terms in $\mathcal{L}_{\phi_i}$ results in the following abstract form:

$$\mathcal{L}_{\phi_i}\delta\phi_i = \underbrace{(\mathtt{I}_1 + \mathtt{I}_2 + \mathtt{I}_{3,3} - \mathtt{I}_{5,1} + \mathtt{I}_6)}_{\texttt{in } \Omega\times(0,T]} + \underbrace{(\mathtt{I}_4 - \mathtt{I}_{3,1})}_{\texttt{on } \Gamma_t\times(0,T]} - \underbrace{\mathtt{I}_{3,2}}_{\texttt{on } \Gamma_u\times(0,T]}\ \underbrace{(-\mathtt{I}_{5,1} + \mathtt{I}_6)}_{\texttt{in } \Omega} + \underbrace{\mathtt{I}_{5,2}}_{\texttt{on } \Gamma} = 0 \tag{29}$$

Since $\boldsymbol{v}_t = \boldsymbol{v}$ on Γ_t, $\mathtt{I}_4$ is equal to $\mathtt{I}_{3,1}$. Because $\boldsymbol{v} = 0$ on Γ_u, $\mathtt{I}_{3,2} = 0$. The last term in (29) vanishes by considering the following boundary conditions for the vector field Φ:

$$\nabla\phi_i(\boldsymbol{x})\cdot\boldsymbol{n}(\boldsymbol{x}) = 0\ \ \texttt{on}\ \ \Gamma,\ \ \texttt{for}\ \ i = 1,\dots p-1 \tag{30}$$

Therefore, the directional derivative of $\mathcal{J}^{\varepsilon,\zeta}$ with respect to ϕ_i at every point $\boldsymbol{x} \in \Omega$ that is denoted by $\mathcal{J}_i'$ (for $i = 1, \ldots, p-1$) can be computed by the following equation:

$$\mathcal{J}_i'(\boldsymbol{x}) = -\zeta\varepsilon\ \Delta\big(\phi_i(\boldsymbol{x})\big) + \frac{\zeta}{\varepsilon}\ W'\big(\phi_i(\boldsymbol{x})\big) + \int_0^T g_i(\boldsymbol{x},t)\ dt \tag{31}$$

where

$$g_i(\boldsymbol{x},t) = \frac{1}{2}\ \rho_{\phi_i}\ \dot{\boldsymbol{u}}^2\ +\ \frac{1}{2}\ \big(\boldsymbol{C}_{\phi_i} : \mathcal{D}(\boldsymbol{u})\big) : \mathcal{D}(\boldsymbol{u})\ +\ \rho_{\phi_i}\ \boldsymbol{v}\cdot\ddot{\boldsymbol{u}}\ +\ \nabla\boldsymbol{v} : \boldsymbol{C}_{\phi_i} : \mathcal{D}(\boldsymbol{u}) \tag{32}$$

Using the identify (23) results in:

$$g_i(\boldsymbol{x},t) = \frac{1}{2}\ \rho_{\phi_i}\ \dot{\boldsymbol{u}}^2\ +\ \frac{1}{2}\ \big(\boldsymbol{C}_{\phi_i} : \mathcal{D}(\boldsymbol{u})\big) : \mathcal{D}(\boldsymbol{u})\ +\ \rho_{\phi_i}\ \boldsymbol{v}\cdot\ddot{\boldsymbol{u}}\ +\ \mathcal{D}(\boldsymbol{v}) : \boldsymbol{C}_{\phi_i} : \mathcal{D}(\boldsymbol{u}) \tag{33}$$

3.3. **First order necessary optimality conditions.** Assume that vector field $\Phi^* = (\phi_1^*, \ldots, \phi_{p-1}^*)$ denotes a constrained stationary point of the objective functional $\mathcal{J}^{\varepsilon,\zeta}$, i.e. a point that satisfies the first order necessary optimality conditions of the optimization problem (11). Considering results presented in subsections 3.1 and 3.2, the first order necessary optimality conditions of problem (11) based on the projected gradient approach can be expressed as follows:

$$\mathscr{P}_{\mathcal{A}}[\Phi^* - \mathcal{J}'] - \Phi^* = 0 \ \texttt{ in } \Omega, \quad \texttt{subject to :}\ \ (1)\ \texttt{ and }\ (28), \tag{34}$$

where $\mathcal{J}' = (\mathcal{J}_1', \ldots, \mathcal{J}_{p-1}')^T$, $\mathcal{J}_i'$ (for $i = 1, \ldots, p-1$) is computed based on (31) and $\mathscr{P}_{\mathcal{A}}$ denotes the orthogonal projection operator onto the convex set $\mathcal{A}$.

4. Regularized projected gradient flow minimization algorithm

Following [37], the regularized projected steepest descent algorithm is used to solve (11) in the present study. In this method, the objective functional is decomposed into non-convex, $\mathcal{J}_N^{\varepsilon,\zeta}$, and convex, $\mathcal{J}_C^{\varepsilon,\zeta}$, parts as follows:

$$\mathcal{J}^{\varepsilon,\zeta}\big(\Phi, \boldsymbol{u}(\Phi)\big) = \mathcal{J}_N^{\varepsilon,\zeta}\big(\Phi, \boldsymbol{u}(\Phi)\big) + \mathcal{J}_C^{\varepsilon,\zeta}(\Phi)$$

where,

$$\mathcal{J}_N^{\varepsilon,\zeta}\big(\Phi, \boldsymbol{u}(\Phi)\big) := \mathcal{J}\big(\Phi, \boldsymbol{u}(\Phi)\big) + \frac{\zeta}{\varepsilon}\ \sum_{i=1}^{p-1} \int_\Omega W(\phi_i)\ d\boldsymbol{x}$$

$$\mathcal{J}_C^{\varepsilon,\zeta}(\Phi) := \frac{\zeta\varepsilon}{2}\ \sum_{i=1}^{p-1} \int_\Omega |\nabla\phi_i|^2\ d\boldsymbol{x}$$

Using the similar approach introduced in section 3, the first variation of $\mathcal{J}_N^{\varepsilon,\zeta}$ and $\mathcal{J}_C^{\varepsilon,\zeta}$, that are respectively denoted by $\mathcal{J}_N'$ and $\mathcal{J}_C'$ here, are computed as follows:

$$\mathcal{J}_N' = (\mathcal{J}_{N1}', \ldots, \mathcal{J}_{Np-1}')^T, \ \ \mathcal{J}_{Ni}'(\boldsymbol{x}) = \frac{\zeta}{\varepsilon}\ W'\big(\phi_i(\boldsymbol{x})\big) + \int_0^T g_i(\boldsymbol{x},t)\ dt \ \texttt{ in }\ \Omega, \ \texttt{ for }\ i = 1, \ldots, p-1 \tag{35}$$

$$\mathcal{J}_C' = (\mathcal{J}_{C1}', \ldots, \mathcal{J}_{Cp-1}')^T, \ \ \mathcal{J}_{Ci}'(\boldsymbol{x}) = -\zeta\varepsilon\ \Delta\phi_i(\boldsymbol{x}) \ \texttt{ in }\ \Omega, \ \texttt{ for }\ i = 1, \ldots, p-1 \tag{36}$$

with boundary conditions (30).

Every iteration of the regularized steepest descent method includes two sequential steps. At the first step, the following optimization problem is solved for one iteration using the projected steepest descent algorithm that is discussed in section 3:

$$\min_{(\Phi,\ \boldsymbol{u})\ \in\ (\mathcal{A},\ \mathcal{U})} \mathcal{J}_N^{\varepsilon,\zeta}\big(\Phi, \boldsymbol{u}(\Phi)\big) \quad \texttt{subject to :}\ \ \texttt{equation}\ \ (1) \tag{37}$$

where the current value of Φ is used as the initial guess in this step. Then, the following optimization problem is solved for one iteration by the Euler implicit algorithm using the current solution of (37) as the initial guess and with boundary conditions (30):

$$\min_{\Phi \in \mathcal{A}} \mathcal{J}_C^{\varepsilon,\zeta}(\Phi) \tag{38}$$

This optimization procedure can be algorithmically stated as follows (c.f. [37, 70] for further details):

Algorithm 1. Regularized projected steepest descent

Step 0. Initialization: given Ω, Γ_u, Γ_f, Γ_t, $\hat{\boldsymbol{u}}$, $\hat{\boldsymbol{t}}$, $\boldsymbol{f}$, p, q, ε, ζ, ρ_i, $\boldsymbol{C}_i$, Λ_i (for $i = 1, \dots, p$), initial guess Φ_0 and stopping criteria parameters δ and k^{max}. If $\Phi_0 \notin \mathcal{A}$ then $\Phi_0 = \mathscr{P}_{\mathcal{A}}[\Phi_0]$, set $k \to 0$.

Step 1. Iterations

1.1 For given Φ_k, solve the direct PDE (1) for $\boldsymbol{u}_k$, and then solve the adjoint PDE (28) for $\boldsymbol{v}_k$.

1.2 For given $\boldsymbol{u}_k$ and $\boldsymbol{v}_k$, compute $\big(\mathcal{J}'_N\big)_k$ by (35). Then, given Φ_k compute Ψ_k by the following equation ($\Psi_k = \big((\psi_1, \dots, \psi_{p-1})^T\big)_k$):

$$\Psi_k = \Phi_k + \alpha_k \bigg(\mathscr{P}_{\mathcal{A}}\big[\Phi_k - \big(\mathcal{J}'_N\big)_k\big] - \Phi_k \bigg) \tag{39}$$

1.3 For given Ψ_k, compute Φ_{k+1} by the following equation with zero-flux boundary conditions:

$$\Phi_{k+1} = \big(\boldsymbol{\mathcal{I}} - \alpha_k \zeta \varepsilon \, \boldsymbol{\Delta}\big)^{-1} \Psi_k \tag{40}$$

Step 2. Stopping criteria: If $k = k^{max}$ or $\|\Phi_{k+1} - \Phi_k\|_{(L^2(\Omega))^{p-1}} < \delta$ stop and return Φ_{k+1} as the optimal solution, else set $k \to k+1$ and goto step 1.

where $\boldsymbol{\mathcal{I}} = (\mathcal{I}_1, \dots, \mathcal{I}_{p-1})^T$, $\mathcal{I}$ denotes the identity operator, $\boldsymbol{\Delta} = (\Delta_1, \dots, \Delta_{p-1})^T$ and $\alpha_k \in (0, 1]$ denotes the stepsize of optimization. The stepsize α_k should be computed based on a globalization strategy to ensure the global convergence of algorithm 1 to a local solution of (11). However, similar to [37] the constant value $\alpha_k = 0.5$ is used in all of our numerical experiments in the present study. Note that (40) is resulted from the Euler implicit time integration of gradient flow equation corresponding to functional $\mathcal{J}_C^{\varepsilon,\zeta}$ (c.f. [37] for further details). As it is shown in [37], (40) lifts the solution from $(L^2(\Omega))^{p-1}$ to $(H^1(\Omega))^{p-1}$, i.e. it regularizes the solution. Furthermore, as it is proved in [37], if $\Phi_k \in \mathcal{A}$ and $\alpha_k \in (0, 1]$ then Φ_{k+1} will lie in $\mathcal{A}$ in step 1 of algorithm 1.

The projection of an arbitrary point onto $\mathcal{A}$ is equivalent to the solution of a quadratic programming (QP) problem (c.f. [69]) which is expensive to solve in general. However, as it is shown in [68, 70], by exploiting the specific structure of $\mathcal{A}$, this problem can be solved very efficiently with a linear computational complexity algorithm. The algorithm #1 of [68] is used to solve this problem in the present study (c.f. section 3.1 of [70]). For the sake of reader convenience this algorithm is briefly mentioned here.

It is obvious that $\mathcal{A}$ lies at the intersection of the following sets:

$$\mathcal{A}_1 := \big\{ \boldsymbol{a} = (a_1, \dots, a_{p-1})^T \in \big(L^2(\Omega)\big)^{p-1} \;\big|\; 0 \leqslant \sum_{i=1}^{p-1} a_i \leqslant 1 \big\}$$

$$\mathcal{A}_2 := \big\{ \boldsymbol{a} = \{a_1, \dots, a_{p-1}\} \in \big(L^2(\Omega)\big)^{p-1} \;\big|\; \int_\Omega a_i \, d\boldsymbol{x} = \Lambda_i |\Omega|, \quad i = 1, \dots, p-1 \big\}$$

$$\mathcal{A}_3 := \big\{ \boldsymbol{a} = \{a_1, \dots, a_{p-1}\} \in \big(L^2(\Omega)\big)^{p-1} \;\big|\; 0 \leqslant a_i \leqslant 1, \quad i = 1, \dots, p-1 \big\}$$

i.e. $\boldsymbol{A} = \boldsymbol{A}_1 \cap \boldsymbol{A}_2 \cap \boldsymbol{A}_3$. It is easy to show that the projection of an arbitrary point $\boldsymbol{a} \in \left(L^2(\Omega)\right)^{p-1}$ onto $\boldsymbol{A}_1$, $\boldsymbol{A}_2$ and $\boldsymbol{A}_3$ are convex separable optimization problems with the following explicit solutions (cf. ch. 10 of [85], ch. 8 of [88], [68]):

$$\mathscr{P}_{\mathcal{A}_1}[\boldsymbol{a}] = \{b_1, \ldots, b_{p-1}\}, \quad b_i = a_i - \frac{\min\left(\sum_{j=1}^{p-1} a_j,\ 0\right)}{p-1} - \frac{\min\left(1 - \sum_{j=1}^{p-1} a_j,\ 0\right)}{p-1}, \quad i = 1, \ldots, p-1$$

$$\mathscr{P}_{\mathcal{A}_2}[\boldsymbol{a}] = \{b_1, \ldots, b_{p-1}\}, \quad b_i = a_i + \Lambda_i - \frac{1}{|\Omega|}\int_\Omega a_i \, d\boldsymbol{x}, \quad i = 1, \ldots, p-1$$

$$\mathscr{P}_{\mathcal{A}_3}[\boldsymbol{a}] = \{b_1, \ldots, b_{p-1}\}, \quad b_i = \max(0,\ \min(a_i,\ 1)), \quad i = 1, \ldots, p-1$$

The projection of trial point $\boldsymbol{a} \in \left(L^2(\Omega)\right)^{p-1}$ onto $\mathcal{A}$ is computed by the following algorithm:

Algorithm 2. Projection onto $\mathcal{A}$

Step 0. Initialization: given Ω, $\mathcal{A}_1$, $\mathcal{A}_2$, $\mathcal{A}_3$, $\boldsymbol{a}$, $\delta > 0$, k^{max}. Set $k \to 0$ and $\boldsymbol{b}_0 = \boldsymbol{a}$.

Step 1. Iterations: $\boldsymbol{b}_{k+1} = \mathscr{P}_{\mathcal{A}_3}\left[\mathscr{P}_{\mathcal{A}_2}\left[\mathscr{P}_{\mathcal{A}_1}[\boldsymbol{b}_k]\right]\right]$, Set $k \to k+1$.

Step 2. Stopping criteria: If $k = k^{max}$ or $\|\boldsymbol{b}_{k+1} - \boldsymbol{b}_k\|_{(L^2(\Omega))^{p-1}} < \delta$ stop and set $\mathscr{P}_{\mathcal{A}}[\boldsymbol{a}] \to \boldsymbol{b}_{k+1}$, else set $k \to k+1$ and goto step 1.

Considering the convexity of $\boldsymbol{A}_1$, $\boldsymbol{A}_2$ and $\boldsymbol{A}_3$, the convergence of algorithm 2 is directly followed by the convergence theory of alternating projection algorithm (c.f. [89, 90])

5. The spatio-temporal discretization

The discretization of physical domain and introduction of appropriate solution algorithms for equations (1), (28) and (40) are the remainder parts of numerical solution corresponding to the optimization problem (11). These issues are discussed briefly in this section.

Without the loss of generality, consider Ω as a subset of $\mathbb{R}^2$ henceforth in the present study. Furthermore, assume that Ω is a rectangle with edges equal to nx and ny units along x and y directions respectively. For the purpose of numerical solution, Ω is discretized into a uniform $nx \times ny$ grid with square elements. The sate variables, $\boldsymbol{u}$, $\boldsymbol{v}$, are defined at the vertices of computational elements and the design vector, Φ, is defined at the centers of elements (c.f. [91, 92]). Assume that the finite dimensional counterpart of each field variable is denoted by superscript $(\cdot)^h$. After the spatial discretization $\boldsymbol{u}^h, \boldsymbol{v}^h \in \mathbb{R}^{n_1}$ and $\Phi^h \in \mathbb{R}^{n_2}$, where $n_1 = 2 \times (nx+1) \times (ny+1)$ and $n_2 = p \times nx \times ny$.

The governing direct and adjoint PDEs are discretized by the finite difference and finite element methods in the time and spatial domains respectively. Now, we discuss the solution algorithm to solve the direct PDE. The classical lagrangian bilinear (P1) and piecewise constant (P0) schemes are used to interpolate the state variables and design vector within each computational elements respectively (c.f. [91, 92]). The spatial discretization of the direct PDE via the finite element method results in the following system of ordinary differential equations (cf. [93, 94]):

$$\boldsymbol{M}\ddot{\boldsymbol{u}}^h + \boldsymbol{K}\boldsymbol{u}^h = \boldsymbol{f}^h \tag{41}$$

where $\boldsymbol{M}$ and $\boldsymbol{K}$ denotes the global mass and stiffness matrices respectively, and $\boldsymbol{f}^h$ denotes the global load vector, includes the contribution of body force and boundary conditions. The mass matrix is computed based on the lumped-mass representation approach (c.f. [93]) in the present study. Because the details of commutating $\boldsymbol{M}$, $\boldsymbol{K}$ and $\boldsymbol{f}^h$ are very classic problems in finite element analysis (they can be found in classic finite element books like [93]), they are omitted here for the purpose of brevity. The above system of equations are solved by the finite difference method based on the Newmark scheme (cf. [94]). The reasonable accuracy and unconditional stability are of the

main benefits of the Newmark approach. For this purpose, the temporal domain is discretized into an m number of uniform subdomains with time stepsize τ, i.e. $T = m\tau$. Assume that superscript n counts the time increments. Using the Newmark scheme, the new displacement field, $(\boldsymbol{u}^h)^{n+1}$, is computed from the the current displacement field, $(\boldsymbol{u}^h)^n$, by the following algebraic system of equations:

$$\left(\frac{1}{\beta\tau^2}\ \boldsymbol{M}+\boldsymbol{K}\right)(\boldsymbol{u}^h)^{n+1}=\boldsymbol{M}\ \left(\frac{1}{\beta\tau^2}\ (\boldsymbol{u}^h)^n+\frac{1}{\beta\tau}\ (\dot{\boldsymbol{u}}^h)^n+\frac{1-2\beta}{2\beta}\ (\ddot{\boldsymbol{u}}^h)^n\right)+(\boldsymbol{f}^h)^n \tag{42}$$

where $\beta=\frac{1}{4}$. Because the coefficient matrix at the left hand side of (42) is fixed during the time integration, it is factorized by LU decomposition method at $n=0$ to avoid the expensive matrix inversion procedure at every time step. After solution of (42), $(\dot{\boldsymbol{u}}^h)^{n+1}$ and $(\ddot{\boldsymbol{u}}^h)^{n+1}$ are computed by the following equations:

$$(\dot{\boldsymbol{u}}^h)^{n+1}=\frac{\gamma}{\beta\tau}\ \left((\boldsymbol{u}^h)^{n+1}-(\boldsymbol{u}^h)^n\right)-\frac{\gamma-\beta}{\beta}\ (\dot{\boldsymbol{u}}^h)^n-\frac{\tau(\gamma-2\beta)}{2\beta}\ (\ddot{\boldsymbol{u}}^h)^n \tag{43}$$

$$(\ddot{\boldsymbol{u}}^h)^{n+1}=\frac{1}{\beta\tau^2}\ \left((\boldsymbol{u}^h)^{n+1}-(\boldsymbol{u}^h)^n-\tau\ (\dot{\boldsymbol{u}}^h)^n\right)-\frac{1-2\beta}{2\beta}\ (\ddot{\boldsymbol{u}}^h)^n \tag{44}$$

where $\gamma=\frac{1}{2}$. The initial acceleration field is computed using (41) as follows:

$$(\ddot{\boldsymbol{u}}^h)^0=\boldsymbol{M}^{-1}\ \left((\boldsymbol{f}^h)^0-\boldsymbol{K}(\boldsymbol{u}^h)^0\right)$$

It is worth to mention that the above variant of Newmark scheme is identical to the trapezoidal time integration algorithm. Note that the time history of direct displacement, velocity and acceleration fields are required to solve the adjoint PDE and to compute the gradient of objective functional. For this purpose, we save $(\boldsymbol{u}^h)^n$, $(\dot{\boldsymbol{u}}^h)^n$ and $(\ddot{\boldsymbol{u}}^h)^n$ for $n=0,\ldots,m$ on the hard disk, and restore them whenever they are required. The same time stepsize and numerical scheme are used to solve the adjoint PDE in the present study. Because the numerical solution of adjoint PDE is similar to the direct PDE, it is not discussed here for the purpose of brevity.

Although the Newmark scheme is unconditionally stable, the choice of τ is a delicate issue in practice. Because the initial conditions of the adjoint PDE is computed based on the terminal solution of the direct PDE, using a large τ leads to significant errors in the input data of adjoint PDE. As a result, the solution of adjoint problem includes significant errors. Consequently, the gradient of objective functional $\mathcal{J}_N^{\varepsilon,\zeta}$ will be inaccurate that can lead to the divergence of optimization procedure. According to our study, the numerical experiment seems to be the most reliable way to chose τ. Moreover, the smallest physical time scale of the problem of interest poses an upper bound on the maximum value of the allowable time stepsize.

Similar to the design vector, the discretized gradient of functional, $\mathcal{J}_N^{\varepsilon,\zeta}$, denoted by $(\mathcal{J}'_N)^h$, is interpolated on P0 finite elements. The trapezoidal time integration algorithm with the time stepsize τ is used to compute $(\mathcal{J}'_N)^h$ in the present study.

The numerical solution of (40) is identical to the numerical solution of $p-1$ distinct scaler-valued Helmholtz equations. Our numerical method in the present study is similar to [37] that is adapted from [92]. The same spatial discretization and interpolation schemes that are discussed for the direct PDE are used to solve (40) here. To solve (40) by the classical P1 finite element method, it is required to have Ψ_k on vertices of P1 finite elements. On the other hand, Φ_k and Ψ_k are interpolated on P0 finite elements. Therefore, to solve (40), firstly Ψ_k is interpolated from elements centers to elements vertices by the linear operator $\boldsymbol{T}_F$. Then, (40) is solved by the classical lagrangian finite element method. Finally, the solution of (40) is interpolated back to the elements centers by the operator $\boldsymbol{T}_F^T$ (c.f. [92] for further details). Because $\alpha_k\zeta\varepsilon$ is constant in the present study, the Helmholtz operator is fixed during our optimization cycles. Therefore, we compute the LU decomposition of discretized Helmholtz operator at the start of optimization and use it during the iterations to avoid $p-1$ number of matrix inversion per optimization cycle.

6. Numerical results and discussion

The success and performance of the presented algorithm will be studied in this section by means of numerical experiments. A personal computer with an AMD 2.4 GHz and 2.5 GB DDR2 RAM is used as the computational resource in the present work. Following [34], a simple model problem is constructed to evaluate the presented algorithm in this study. The geometry and boundary conditions corresponding to this model problem are shown in figure 1. The load $F(t)$ in figure 1 varies with time based on a gaussian distribution in time domain, more precisely,

$$F(t) = \exp\big(\frac{-(t-t_0)^2}{2\sigma^2}\big)$$

where $t_0 = 10$ and $\sigma = 2$ here, as illustrated in figure 2. To reduce the computational cost, the symmetry of this model problem is taken into account during our simulations (however, the numerical results are presented on the full domain for the sake of convenience). Assume that the poisson ratio and Young's modulus of i-th material are denoted by ν_i and E_i respectively. Following [36, 55, 92], it is assumed that $\nu_1 = \cdots = \nu_p = 0.3$. Therefore, the elasticity tensor of i-th material can be written as $E_i\mathbf{C}_0$, where $\mathbf{C}_0$ denotes the elasticity tensor of a material with $\nu = 0.3$ and $E = 1$. The computational domain is divided into a uniform 20×10 squared elements with the unit edge length (the computational domain here is equal to one half of the physical domain by exploiting the symmetry of Ω). The problem is solved in temporal domain $(0, 40]$ with time stepsize $\tau = 1$. The penalization factor, q, and the regularization parameter, ε, are respectively equal to 3 and 1 in our numerical experiments. In fact ε is equal to the element size here. Note that smaller values for ε is not recommended in the literature. To evaluate the presented algorithm, 12 test problems are considered in this section. In all cases, the optimization is terminated after 500 iterations, i.e. $k^{max} = 500$ and $\delta = 0$ in algorithm 1. Furthermore, $\delta = 10^{-14}$ and $k^{max} = \infty$ in algorithm 2. The overall volume fractions of all phases are assumed to be equal in all test problems, i.e. $\Lambda_i = 1/p$ $(i = 1, \ldots, p-1)$. Table 1 shows the remained simulation parameters corresponding to test cases #1-#12. Following [36], the distribution of phases are shown by making a bitmap image in which a distinct color is attributed to each material. More precisely, the background phase (the weakest phase) is shown by the white color and remaining phases are shown by red, green, blue, yellow, colors respectively based on the descending order of E. A uniform material distribution is considered as the initial design in all test cases in the present study, i.e. $\Phi_0 = 1/p$.

The variation of different parts of objective functional in addition to its total value with iterations are shown in figures 3 and 4 for test cases #1, #5, #8 and #12. According to the plots, the objective functional $\mathcal{J}^{\varepsilon,\zeta}$ decreases monotonically as iterations proceed, and its variations decay with iterations. This observation confirms the convergence and feasibility of the presented algorithm in practice. Furthermore, all parts of objective functionals, i.e. potential energy, kinetic energy and perimeter; almost reduce monotonically with iterations. It is important to note that the total stored energy in the structure is decreased by more than an order of magnitude after a few number of optimization cycles. This observation implies the practical importance of the optimal design problem considered in this study. According to these plots, the total value of stored kinetic energy in the structure is comparable to that of the potential energy. Therefore, unlike [22] that considered only the potential part of the stored energy, both parts should be taken into account to find a more reliable design. The same trends are observed in the other cases that are not reported here. Because, no internal dissipation mechanism considered in the present study, the elastic energy is transmitted to the environment through the fixed displacement boundaries.

The evolution of topologies with iterations are shown in figures 5-8 for test cases #1-#12. According to these figures, the presented algorithm was successful to generate nearly 0-1 topologies without regard to the number of phases. This observation moderates the mentioned challenge corresponding to the optimal design of multiphase structures due to the lack of multiphase constitutive equation. According to figures 5-8, increasing the perimeter penalization parameter ζ, increases the sharpness of final topologies. Moreover, the total perimeter of boundaries between phases decreases by increasing of this parameter. However, it should be chosen with care to avoid undesirable results.

A clue in this regard is to compute the value of $\frac{\mathcal{J}}{\zeta P^{\varepsilon}}$ at the start of optimization. If this parameter is too small, ζ should be decreased. On the other hand, ζ should be increased when it is too large.

To make sense about the impact of optimization on the practical behavior of structures, the dynamics of initial and optimal designs corresponding to test cases #6, #9 and #12 are plotted in figures 9-11 (the elastic deformation of bodies are magnified on the plots). Note that it is assumed that the simple constitutive equation used in this study is valid for the initial designs which have not near 0-1 topologies. According to the plots, the deformations of structures, in particular on the free surfaces, are significantly reduced after the design optimization. This outcome reduces the risk of fatigue crack formation on the free surfaces and its propagation inside the structures. According to figures 9-11, the distribution of dilatational stresses in the body is more uniform in the optimal designs. Moreover, the maximum values of the dilatational stresses are reduced as a result of design optimization.

7. Summary

A new computational algorithm is introduced in the present study to solve multimaterial topology optimization problems under elastodynamic loading conditions. The objective functional, to be minimized, is defined as the time-averaged total stored energy in the structure within a finite time interval. To regularize the original optimization problem, the objective functional is penalized by the approximate total perimeter of boundaries between phases. A new approach is developed for the first order adjoint sensitivity analysis of the optimization problems constrained to the linear wave equation. The penalized optimization problem is solved by the regularized projected steepest descent algorithm. The presented algorithm generates solutions with H^1 regularity. Its success is supported by numerical experiments. According to numerical results, the objective functional is reduced monotonically with iterations. It (as well as its penalized form) is reduced more than an order of magnitude after a few iterations (for instance 50 iterations) of the presented algorithm. These observation confirm the practical convergence of the presented method. Considering the contributions of kinetic and potential stored energy in the structure at the initial as well as optimal designs shows that they are comparable to each other. Therefore, both of them should be taken into account unlike some former researches in which only the potential part was considered. The resulted topologies at the optimal solutions are near 0-1. This observation approve the success of the introduced penalization method in practice. Comparing the dynamical behavior of optimal designs to initial ones shows that the displacement of structure and the magnitude of dilatational stresses are significantly decreased as a result of optimization.

References

[1] M.P. Bendsøe and O. Sigmund. *Topology Optimization: theory, methods and applications*. Springer, 2004.

[2] G. Allaire. Shape optimization by the homogenization method. *New York, Springer-Verlag*, 2002.

[3] A. Díaaz and N. Kikuchi. Solutions to shape and topology eigenvalue optimization problems using a homogenization method. *Int J Numer Meth Eng*, 35(7):1487–1502, 1992.

[4] Z. Ma, N. Kikuchi, and I. Hagiwara. Structural topology and shape optimization for a frequency response problem. *Computat Mech*, 13(3):157–174, 1993.

[5] Z. Ma, N. Kikuchi, and H. Cheng. Topological design for vibrating structures. *Comput Meth Appl Mech Eng*, 121(1):259–280, 1995.

[6] H. Du, G. Lau, M. Lim, and J. Qui. Topological optimization of mechanical amplifiers for piezoelectric actuators under dynamic motion. *Smart Mater Struct*, 9(6):788, 2000.

[7] G. Allaire, S. Aubry, and F. Jouve. Eigenfrequency optimization in optimal design. *Comput Meth Appl Mech Eng*, 190(28):3565–3579, 2001.

[8] C. Jog. Topology design of structures subjected to periodic loading. *J Sound Vib*, 253(3):687–709, 2002.

[9] D. Tcherniak. Topology optimization of resonating structures using simp method. *Int J Numer Meth Eng*, 54(11):1605–1622, 2002.

[10] T. Kim, J. Kim, and Y. Kim. Parallelized structural topology optimization for eigenvalue problems. *Int J Solids Struct*, 41(9):2623–2641, 2004.

[11] J. Jensen and N. Pedersen. On maximal eigenfrequency separation in two-material structures: the 1d and 2d scalar cases. *J Sound Vib*, 289(4):967–986, 2006.
[12] Y Maeda, S Nishiwaki, K Izui, M Yoshimura, K Matsui, and K Terada. Structural topology optimization of vibrating structures with specified eigenfrequencies and eigenmode shapes. *Int J Numer Meth Eng*, 67(5):597–628, 2006.
[13] J. Du and N. Olhoff. Topological design of freely vibrating continuum structures for maximum values of simple and multiple eigenfrequencies and frequency gaps. *Struct Multidisc Optim*, 34(2):91–110, 2007.
[14] J. Du and N. Olhoff. Minimization of sound radiation from vibrating bi-material structures using topology optimization. *Struct and Multidisc Optim*, 33(4-5):305–321, 2007.
[15] B. Niu, J. Yan, and G. Cheng. Optimum structure with homogeneous optimum cellular material for maximum fundamental frequency. *Struct Multidisc Optim*, 39(2):115–132, 2009.
[16] M. Stingl, M. Kocvara, and G. Leugering. Free material optimization with fundamental eigenfrequency constraints. *SIAM J Optim*, 20(1):524–547, 2009.
[17] G. Yoon. Structural topology optimization for frequency response problem using model reduction schemes. *Comput Meth Appl Mech Eng*, 199(25):1744–1763, 2010.
[18] J. Du and N. Olhoff. Topological design of vibrating structures with respect to optimum sound pressure characteristics in a surrounding acoustic medium. *Struct Multidisc Optim*, 42(1):43–54, 2010.
[19] M. Bruggi and A. Taliercio. Maximization of the fundamental eigenfrequency of micropolar solids through topology optimization. *Struct Multidisc Optim*, 46(4):549–560, 2012.
[20] A. Takezawa and M. Kitamura. Sensitivity analysis and optimization of vibration modes in continuum systems. *J Sound Vib*, 332(6):1553–1566, 2013.
[21] X. Yang and Y. Li. Topology optimization to minimize the dynamic compliance of a bi-material plate in a thermal environment. *Struct Multidisc Optim*, pages 1–10, 2013.
[22] S. Turteltaub. Optimal non-homogeneous composites for dynamic loading. *Struct Multidisc Optim*, 30(2):101–112, 2005.
[23] B. Kang, G. Park, and J. Arora. A review of optimization of structures subjected to transient loads. *Struct Multidisc Optim*, 31(2):81–95, 2006.
[24] S. Min, N. Kikuchi, Y. Park, S. Kim, and S. Chang. Optimal topology design of structures under dynamic loads. *Struct Optim*, 17(2-3):208–218, 1999.
[25] J. Dahl, J. Jensen, and O. Sigmund. Topology optimization for transient wave propagation problems in one dimension. *Struct Multidisc Optim*, 36(6):585–595, 2008.
[26] F. Maestre, A. Münch, and P. Pedregal. A spatio-temporal design problem for a damped wave equation. *SIAM J Appl Math*, 68(1):109–132, 2007.
[27] A. Münch, P. Pedregal, and F. Periago. Optimal internal stabilization of the linear system of elasticity. *Arch Rat Mech Anal*, 193(1):171–193, 2009.
[28] F. Maestre and P. Pedregal. Dynamic materials for an optimal design problem under the two-dimensional wave equation. *Discrete Contin Dynam Systems A*, 23(3):973–990, 2009.
[29] A. Chambolle and F. Santosa. Control of the wave equation by time-dependent coefficient. *ESAIM: COCV*, 8:375–392, 2002.
[30] J. Jensen. Space–time topology optimization for one-dimensional wave propagation. *Comput Meth Appl Mech Eng*, 198(5):705–715, 2009.
[31] J. Jensen. Optimization of space-time material layout for 1d wave propagation with varying mass and stiffness parameters. *Control Cyber*, 39(3):599–614, 2010.
[32] G. Allaire and A. Kelly. Optimal design of low-contrast two-phase structures for the wave equation. *Math Mod Meth Appl Sci*, 21(07):1499–1538, 2011.
[33] A. Amirkhizi, A. Tehranian, and S. Nemat-Nasser. Stress-wave energy management through material anisotropy. *Wave Motion*, 47(8):519–536, 2010.
[34] C. Le, T. Bruns, and D. Tortorelli. Material microstructure optimization for linear elastodynamic energy wave management. *J Mech Phys Solids*, 60(2):351–378, 2012.
[35] P. Nakshatrala and D. Tortorelli. Topology optimization for effective energy propagation in rate-independent elastoplastic material systems. *Comput Meth Appl Mech Eng*, 2015.
[36] R. Tavakoli and S.M. Mohseni. Alternating active-phase algorithm for multimaterial topology optimization problems: a 115-line matlab implementation. *Struct Multidisc Optim*, 49(4):621–642, 2014.
[37] R. Tavakoli. Multimaterial topology optimization by volume constrained allen–cahn system and regularized projected steepest descent method. *Comput Meth Appl Mech Eng*, 276:534–565, 2014.
[38] O. Sigmund and S. Torquato. Composites with extremal thermal expansion coefficients. *Appl Phys Lett*, 69(21):3203–3205, 1996.

[39] O. Sigmund and S. Torquato. Design of materials with extreme thermal expansion using a three-phase topology optimization method. *J Mech Phys Solids*, 45(6):1037–1067, 1997.
[40] O. Sigmund and S. Torquato. Design of smart composite materials using topology optimization. *Smart Materials and Structures*, 8:365, 1999.
[41] L. Gibiansky and O. Sigmund. Multiphase composites with extremal bulk modulus. *J Mech Phys Solids*, 48(3):461–498, 2000.
[42] G. Allaire and C. Castro. Optimization of nuclear fuel reloading by the homogenization method. *Struct Multidisc Optim*, 24(1):11–22, 2002.
[43] M. Yulin and W. Xiaoming. A level set method for structural topology optimization and its applications. *Adv Eng Softw*, 35(7):415–441, 2004.
[44] M.Y. Wang and X. Wang. color level sets: a multi-phase method for structural topology optimization with multiple materials. *Comput Meth Appl Mech Engng*, 193(6):469–496, 2004.
[45] M.Y. Wang and X. Wang. A level-set based variational method for design and optimization of heterogeneous objects. *Computer-Aided Design*, 37(3):321–337, 2005.
[46] E. Dombre, G. Allaire, O. Pantz, and D. Schmitt. Shape optimization of a sodium fast reactor core. In *ESAIM Proc*, volume 38, pages 319–334. EDP Sciences, 2012.
[47] P. Wei and M. Wang. Piecewise constant level set method for structural topology optimization. *Int J Numer Methods Eng*, 78(4):379–402, 2009.
[48] Z. Luo, L. Tong, J. Luo, P. Wei, and M. Wang. Design of piezoelectric actuators using a multiphase level set method of piecewise constants. *J Comput Phys*, 228(7):2643–2659, 2009.
[49] N. Vermaak, G. Michailidis, G. Parry, R. Estevez, G. Allaire, and Y. Bréchet. Material interface effects on the topology optimizationof multi-phase structures using a level set method. *Struct Multidisc Optim*, 50(4):623–644, 2014.
[50] G. Allaire, C. Dapogny, G. Delgado, and G. Michailidis. Multi-phase structural optimization via a level set method. *ESAIM: COCV*, 20(2):576–611, 2014.
[51] Y. Wang, Z. Luo, Z. Kang, and N. Zhang. A multi-material level set-based topology and shape optimization method. *Comput Meth Appl Mech and Eng*, 283:1570–1586, 2015.
[52] B. Bourdin and A. Chambolle. Design-dependent loads in topology optimization. *ESAIM COCV*, 9:19–48, 2003.
[53] M.Y. Wang and S. Zhou. Synthesis of shape and topology of multi-material structures with a phase-field method. *J Comput-Aided Mater Des*, 11(2):117–138, 2004.
[54] S. Zhou and M. Wang. 3d multi-material structural topology optimization with the generalized cahn-hilliard equations. *CMES: Comput Model in Eng Sci*, 16(2):83–102, 2006.
[55] S. Zhou and M. Wang. Multimaterial structural topology optimization with a generalized cahn–hilliard model of multiphase transition. *Struct Multidisc Optim*, 33(2):89–111, 2007.
[56] L. Blank, H. Garcke, L. Sarbu, and V. Styles. Primal-dual active set methods for allen–cahn variational inequalities with nonlocal constraints. *Numer Meth Partial Differential Equations*, 2012.
[57] L. Blank, H. Garcke, L. Sarbu, T. Srisupattarawanit, V. Styles, and A. Voigt. Phase-field approaches to structural topology optimization. In *Constrained Optimization and Optimal Control for Partial Differential Equations*, pages 245–256. Springer, 2012.
[58] J. Stegmann and E. Lund. Discrete material optimization of general composite shell structures. *Int J Numer Meth Eng*, 62(14):2009–2027, 2005.
[59] E. Lund and J. Stegmann. On structural optimization of composite shell structures using a discrete constitutive parametrization. *Wind Energy*, 8(1):109–124, 2005.
[60] T. Gao and W. Zhang. A mass constraint formulation for structural topology optimization with multiphase materials. *Int J Numer Meth Eng*, 88(8):774–796, 2011.
[61] M. Bruyneel. Sfpa new parameterization based on shape functions for optimal material selection: application to conventional composite plies. *Struct Multidisc Optim*, 43(1):17–27, 2011.
[62] M. Bruyneel, P. Duysinx, C. Fleury, and T.. Gao. Extensions of the shape functions with penalization parameterization for composite-ply optimization. *AIAA J*, 49(10):2325–2329, 2011.
[63] T. Gao, W. Zhang, and P. Duysinx. A bi-value coding parameterization scheme for the discrete optimal orientation design of the composite laminate. *Int J Numer Meth Eng*, 91(1):98–114, 2012.
[64] L. Zhen, G. Wei, and S. Chongmin. Design of multi-phase piezoelectric actuators. *J Intel Mater Sys Struct*, 21(8):1851–1865, 2010.
[65] C. Hvejsel and E. Lund. Material interpolation schemes for unified topology and multi-material optimization. *Struct Multidisc Optim*, 43(6):811–825, 2011.

[66] L. Dedè, M. Borden, and T. Hughes. Isogeometric analysis for topology optimization with a phase field model. *Arch Comput Meth Eng*, 19(3):427–465, 2012.
[67] S. Turteltaub. Optimal control and optimization of functionally graded materials for thermomechanical processes. *Int J Solids Struct*, 39(12):3175–3197, 2002.
[68] R. Tavakoli. On the coupled continuous knapsack problems: projection onto the volume constrained gibbs n-simplex. *Optim Letters*, pages 1–22, 2015.
[69] J. Nocedal and S. Wright. *Numerical optimization*. Springer verlag, 1999.
[70] R. Tavakoli. Computationally efficient approach for the minimization of volume constrained vector-valued ginzburg-landau energy functional. *J Comput Phys*, 295:355–378, 2015.
[71] O. Sigmund and J. Petersson. Numerical instabilities in topology optimization: a survey on procedures dealing with checkerboards, mesh-dependencies and local minima. *Struct Multidisc Optim*, 16(1):68–75, 1998.
[72] R. Haber, C. Jog, and M. Bendsøe. A new approach to variable-topology shape design using a constraint on perimeter. *Struct Optim*, 11(1-2):1–12, 1996.
[73] M. Burger and R. Stainko. Phase-field relaxation of topology optimization with local stress constraints. *SIAM J Control Optim*, 45(4):1447–1466, 2006.
[74] J. Choi, T. Yamada, K. Izui, S. Nishiwaki, and J. Yoo. Topology optimization using a reaction–diffusion equation. *Comput Meth Appl Mech Eng*, 200(29):2407–2420, 2011.
[75] M. Wallin, M. Ristinmaa, and H. Askfelt. Optimal topologies derived from a phase-field method. *Struct Multidisc Optim*, 45(2):171–183, 2012.
[76] A. Gain and G. Paulino. Phase-field based topology optimization with polygonal elements: a finite volume approach for the evolution equation. *Struct Multidisc Optim*, 46(3):327–342, 2012.
[77] P. Penzler, M. Rumpf, and B. Wirth. A phase-field model for compliance shape optimization in nonlinear elasticity. *ESAIM: COCV*, 18(1):229–258, 2012.
[78] L. Modica and S. Mortola. Un esempio di γ-convergenza. *Boll. Un. Mat. Ital. B*, 14(1):285–299, 1977.
[79] L. Modica. The gradient theory of phase transitions and the minimal interface criterion. *Arch Rat Mech Anal*, 98(2):123–142, 1987.
[80] S. Baldo. Minimal interface criterion for phase transitions in mixtures of cahn-hilliard fluids. *Ann Inst H. Poincaré (C) Anal Non Linéaire*, 7(2):67–90, 1990.
[81] E. Oudet. Approximation of partitions of least perimeter by γ-convergence: around kelvins conjecture. *Exp Math*, 20(3):260–270, 2011.
[82] R. Tavakoli and H. Zhang. A nonmonotone spectral projected gradient method for large-scale topology optimization problems. *Numer Algebra, Control Optim*, 2(2):395–412, 2012.
[83] E. Birgin, J. Martínez, and M. Raydan. Nonmonotone spectral projected gradient methods on convex sets. *SIAM J Optim*, 10(4):1196–1211, 2000.
[84] D. Tortorelli and P. Michaleris. Design sensitivity analysis: overview and review. *Inverse Probl Eng*, 1(1):71–105, 1994.
[85] G. Allaire. *Numerical analysis and optimization: an introduction to mathematical modelling and numerical simulation*. Translated by: Craig, A., Oxford University Press, USA, 2007.
[86] F. Tröltzsch. *Optimal control of partial differential equations: Theory, methods and applications*, volume 112. AMS Bookstore, 2010.
[87] A. Borzi and V. Schulz. *Computational optimization of systems governed by partial differential equations*. SIAM, 2012.
[88] S. Boyd and L. Vandenberghe. *Convex optimization*. Cambridge university press, 2004.
[89] S. Boyd and J. Dattorro. Alternating projections. *Online note*, 2003. is available online at: `web.stanford.edu/class/ee392o/alt_proj.pdf`.
[90] R. Escalante and M. Raydan. *Alternating Projection Methods*, volume 8. SIAM, 2011.
[91] O. Sigmund. A 99 line topology optimization code written in matlab. *Struct Multidisc Optim*, 21(2):120–127, 2001.
[92] E. Andreassen, A. Clausen, M. Schevenels, B. Lazarov, and O. Sigmund. Efficient topology optimization in matlab using 88 lines of code. *Struct Multidisc Optim*, 43(1):1–16, 2011.
[93] J. Przemieniecki. *Theory of matrix structural analysis*. Courier Dover Publications, 1985.
[94] T. Belytschko, B. Moran, and W. Liu. *Nonlinear finite element analysis for continua and structures*, volume 1. Wiley, 1999.

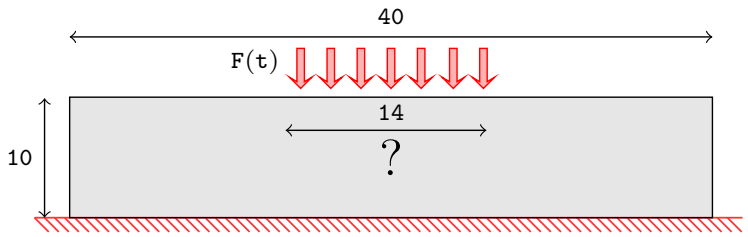

FIGURE 1. The geometry and boundary conditions of the model problem in this study.

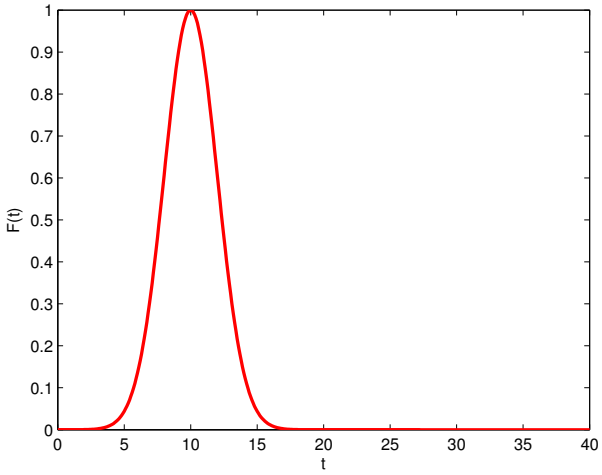

FIGURE 2. The variation of $F(t)$ with time in the present study.

ID of Test Case	p	ζ	Young's Modulus	Density	Volume Fraction
#1	2	0.1	[1000 100]	[1000 100]	[1/2 1/2]
#2	2	0.5	[1000 100]	[1000 100]	[1/2 1/2]
#3	2	1.0	[1000 100]	[1000 100]	[1/2 1/2]
#4	3	0.1	[1000 100 10]	[1000 100 10]	[1/3 1/3 1/3]
#5	3	0.5	[1000 100 10]	[1000 100 10]	[1/3 1/3 1/3]
#6	3	1.0	[1000 100 10]	[1000 100 10]	[1/3 1/3 1/3]
#7	4	0.1	[1000 100 10 1]	[1000 100 10 1]	[1/4 1/4 1/4 1/4]
#8	4	0.5	[1000 100 10 1]	[1000 100 10 1]	[1/4 1/4 1/4 1/4]
#9	4	1.0	[1000 100 10 1]	[1000 100 10 1]	[1/4 1/4 1/4 1/4]
#10	5	0.1	[1000 100 10 1 0.1]	[1000 100 10 1 0.1]	[1/5 1/5 1/5 1/5 1/5]
#11	5	0.5	[1000 100 10 1 0.1]	[1000 100 10 1 0.1]	[1/5 1/5 1/5 1/5 1/5]
#12	5	1.0	[1000 100 10 1 0.1]	[1000 100 10 1 0.1]	[1/5 1/5 1/5 1/5 1/5]

TABLE 1. Design parameters corresponding to test problems #1-#12 in the present study.

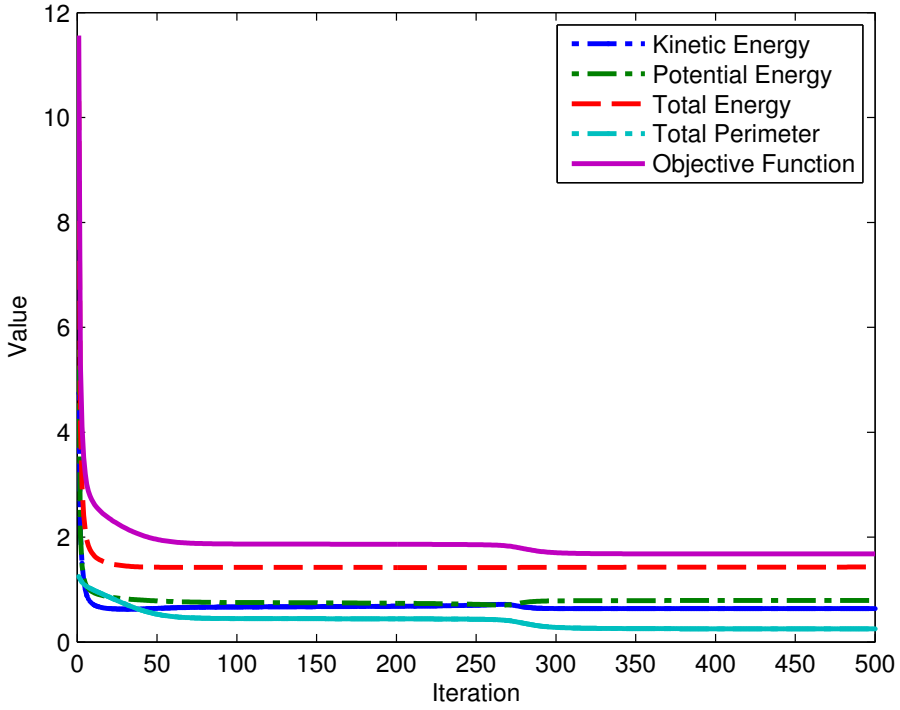

(a) test case #1

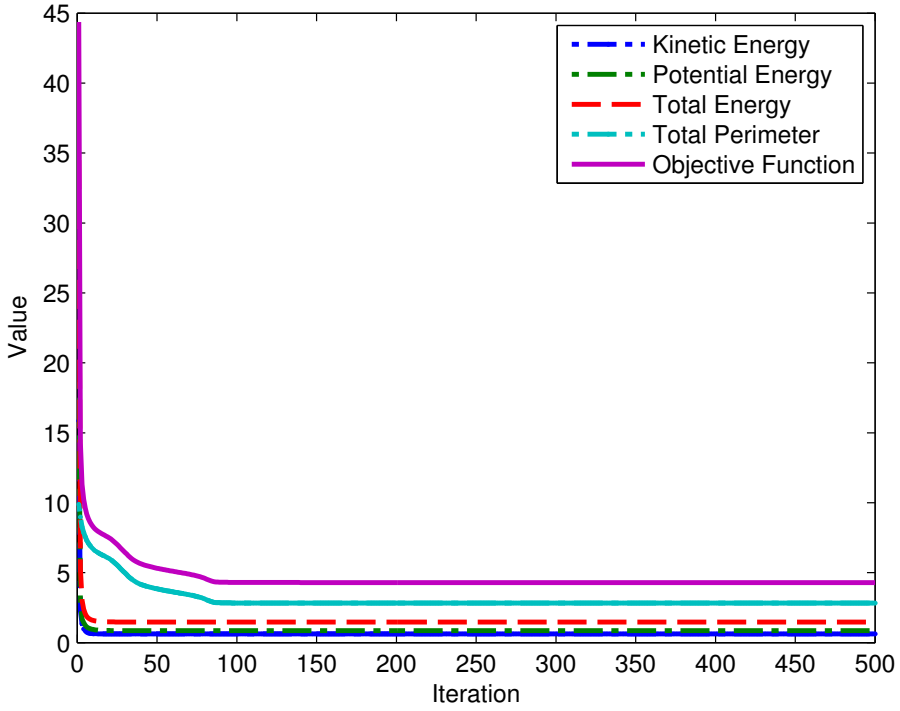

(b) test case #5

FIGURE 3. Variation of objective functional and its components as a function of iterations, for test cases #1 and #5.

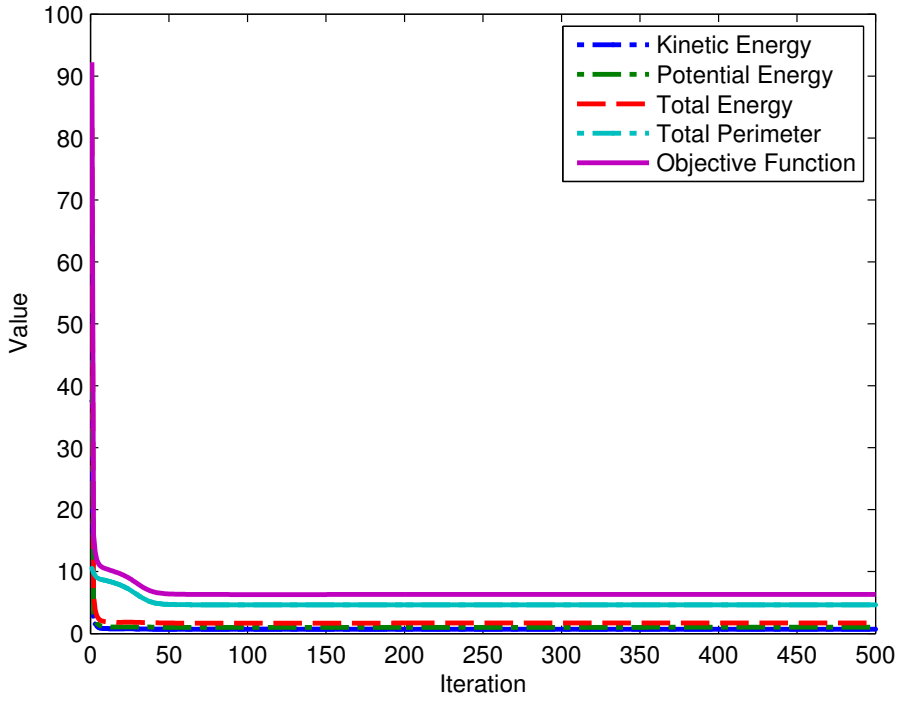

(a) test case #8

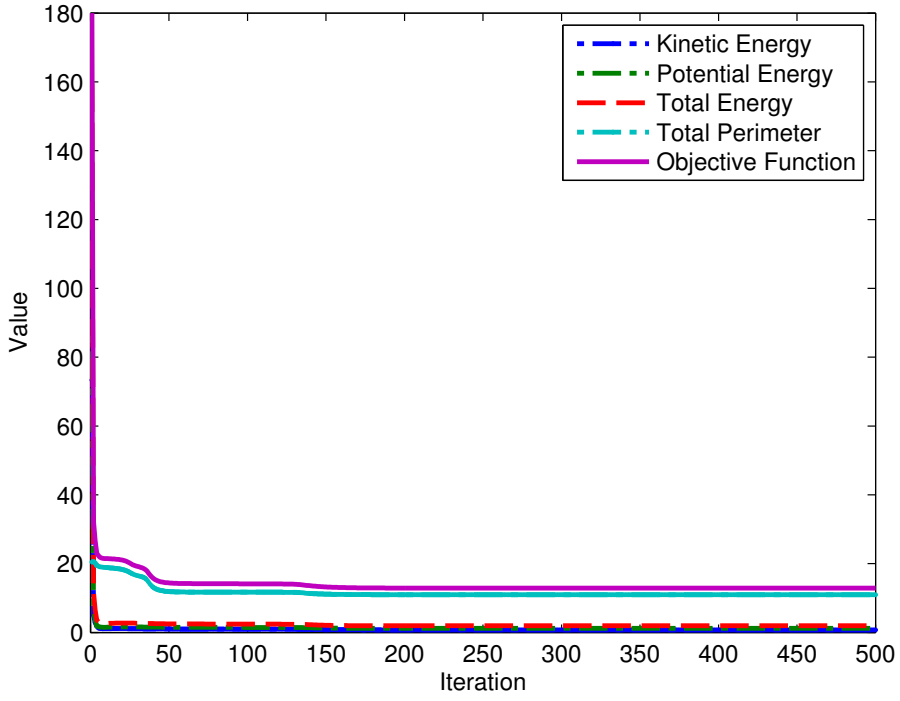

(b) test case #12

FIGURE 4. Variation of objective functional and its components as a function of iterations, for test cases #8 and #12.

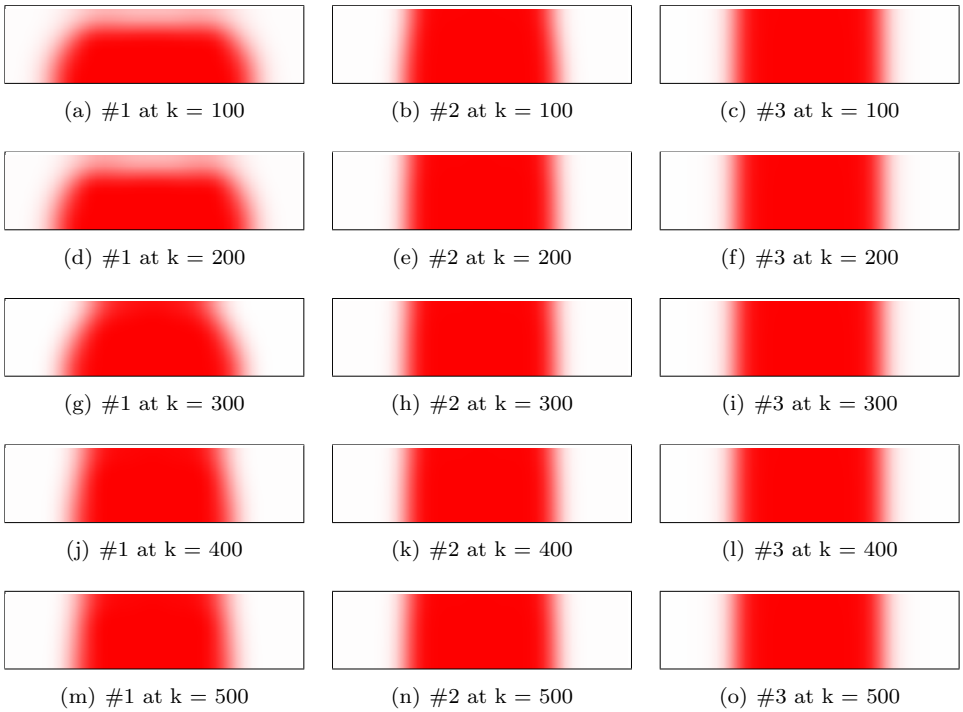

(a) #1 at k = 100 (b) #2 at k = 100 (c) #3 at k = 100

(d) #1 at k = 200 (e) #2 at k = 200 (f) #3 at k = 200

(g) #1 at k = 300 (h) #2 at k = 300 (i) #3 at k = 300

(j) #1 at k = 400 (k) #2 at k = 400 (l) #3 at k = 400

(m) #1 at k = 500 (n) #2 at k = 500 (o) #3 at k = 500

FIGURE 5. Evolution of topologies corresponding to test case #1-#3.

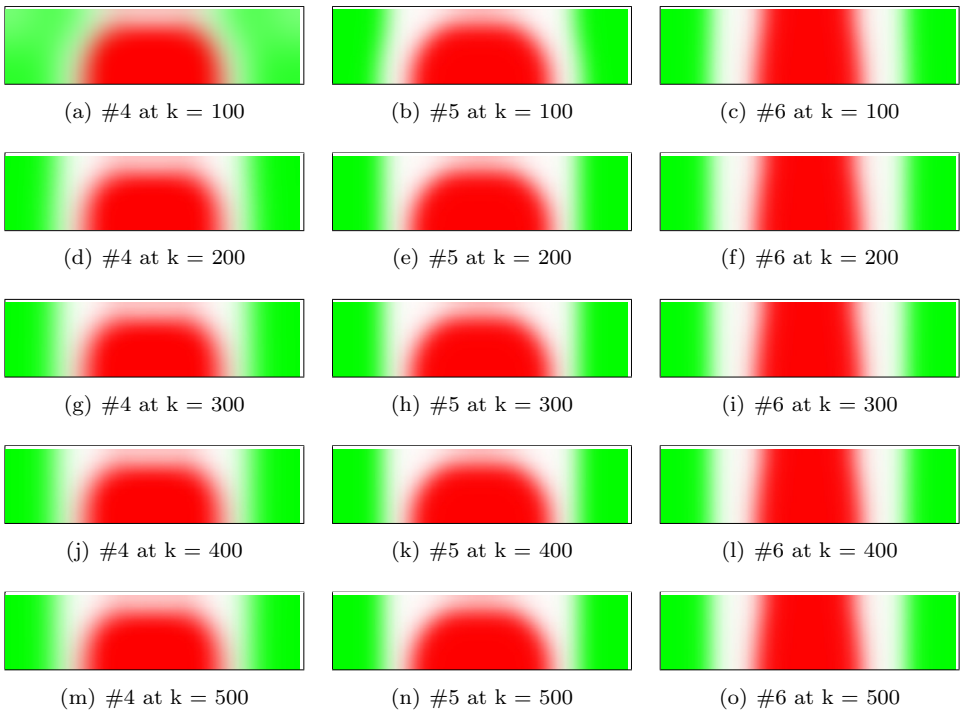

(a) #4 at k = 100 (b) #5 at k = 100 (c) #6 at k = 100

(d) #4 at k = 200 (e) #5 at k = 200 (f) #6 at k = 200

(g) #4 at k = 300 (h) #5 at k = 300 (i) #6 at k = 300

(j) #4 at k = 400 (k) #5 at k = 400 (l) #6 at k = 400

(m) #4 at k = 500 (n) #5 at k = 500 (o) #6 at k = 500

FIGURE 6. Evolution of topologies corresponding to test case #4-#6.

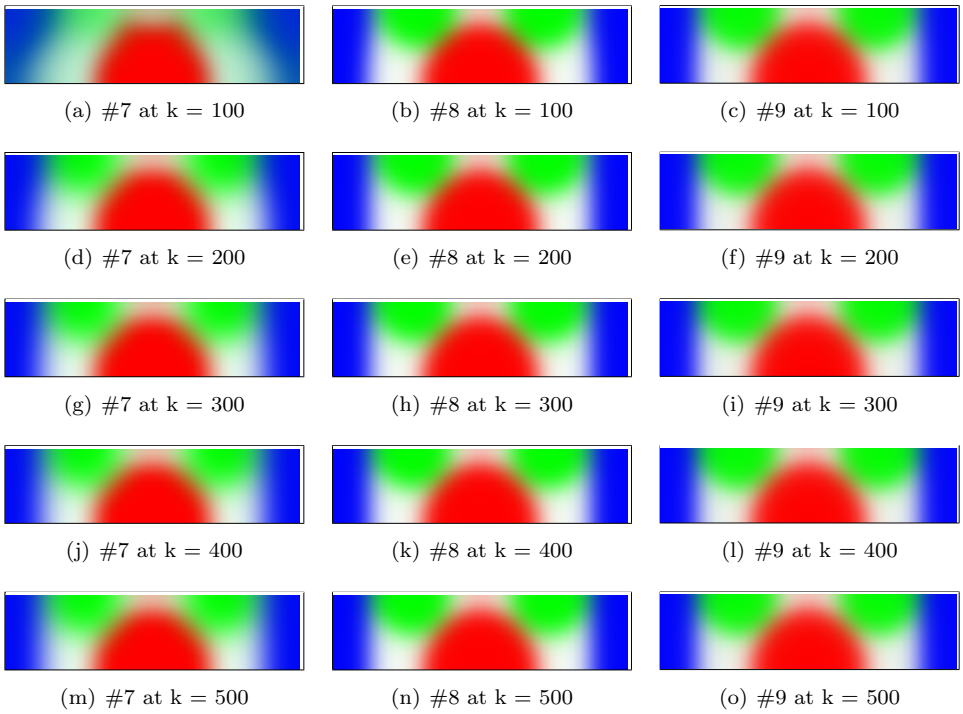

(a) #7 at k = 100 (b) #8 at k = 100 (c) #9 at k = 100

(d) #7 at k = 200 (e) #8 at k = 200 (f) #9 at k = 200

(g) #7 at k = 300 (h) #8 at k = 300 (i) #9 at k = 300

(j) #7 at k = 400 (k) #8 at k = 400 (l) #9 at k = 400

(m) #7 at k = 500 (n) #8 at k = 500 (o) #9 at k = 500

FIGURE 7. Evolution of topologies corresponding to test case #7-#9.

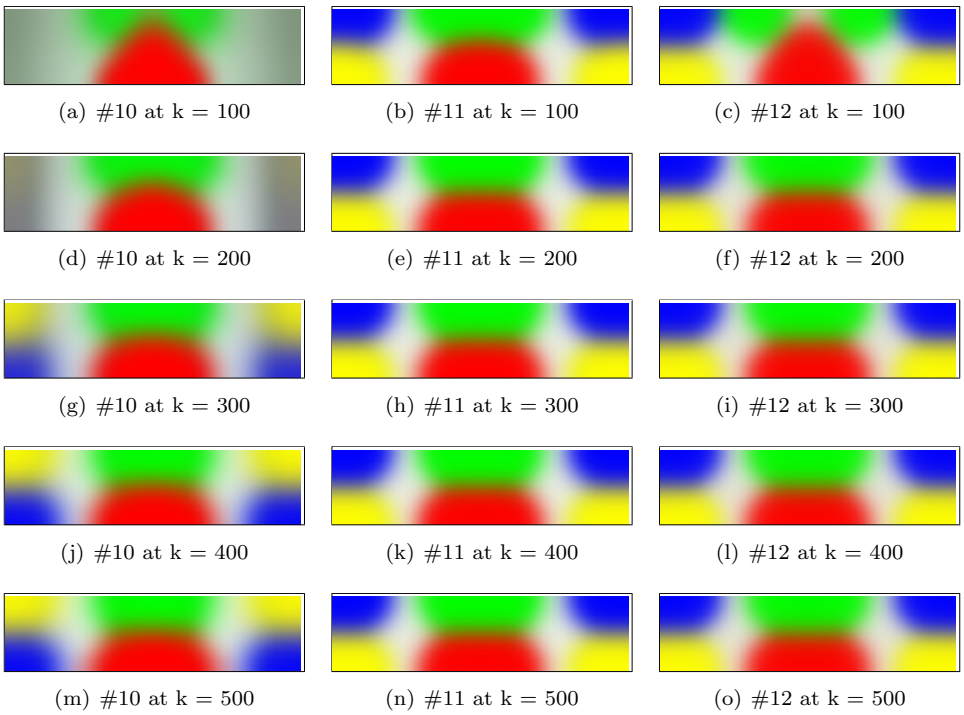

(a) #10 at k = 100 (b) #11 at k = 100 (c) #12 at k = 100

(d) #10 at k = 200 (e) #11 at k = 200 (f) #12 at k = 200

(g) #10 at k = 300 (h) #11 at k = 300 (i) #12 at k = 300

(j) #10 at k = 400 (k) #11 at k = 400 (l) #12 at k = 400

(m) #10 at k = 500 (n) #11 at k = 500 (o) #12 at k = 500

FIGURE 8. Evolution of topologies corresponding to test case #10-#12.

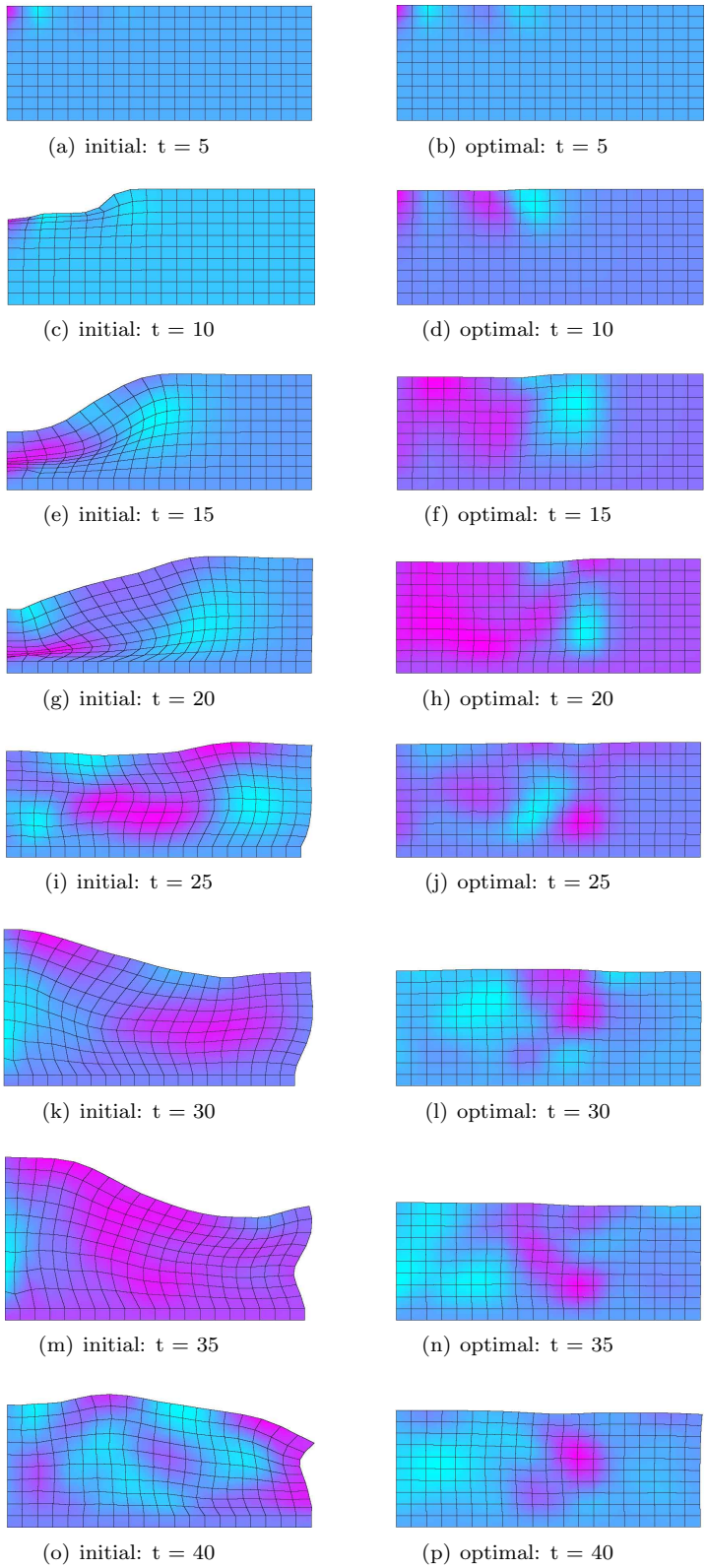

(a) initial: t = 5 (b) optimal: t = 5

(c) initial: t = 10 (d) optimal: t = 10

(e) initial: t = 15 (f) optimal: t = 15

(g) initial: t = 20 (h) optimal: t = 20

(i) initial: t = 25 (j) optimal: t = 25

(k) initial: t = 30 (l) optimal: t = 30

(m) initial: t = 35 (n) optimal: t = 35

(o) initial: t = 40 (p) optimal: t = 40

FIGURE 9. The elastic deformation of structure with time for initial and optimal designs of test case #6. The displacements are magnified by factor 40 for the better illustration. Contours show the distribution of dilatation stress inside the structure.

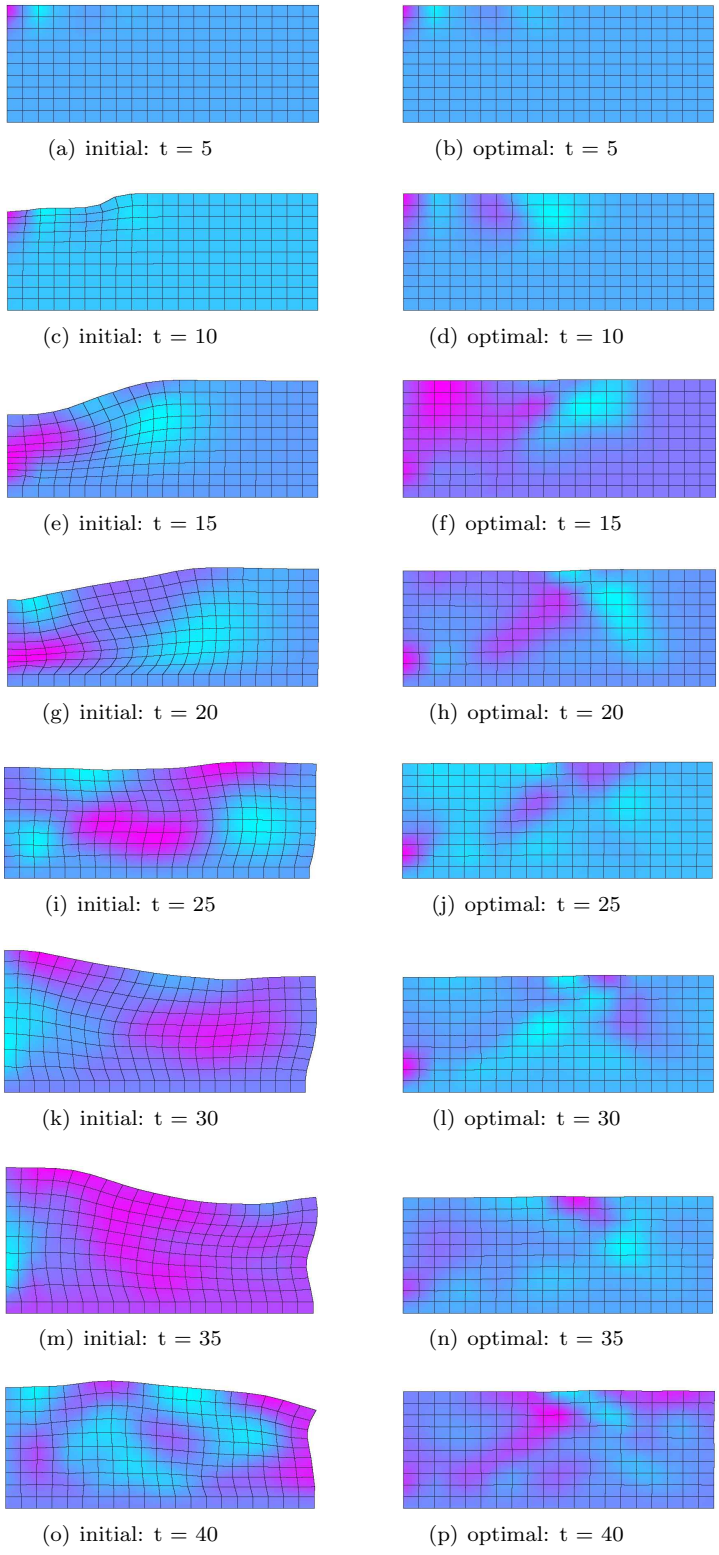

(a) initial: t = 5 (b) optimal: t = 5

(c) initial: t = 10 (d) optimal: t = 10

(e) initial: t = 15 (f) optimal: t = 15

(g) initial: t = 20 (h) optimal: t = 20

(i) initial: t = 25 (j) optimal: t = 25

(k) initial: t = 30 (l) optimal: t = 30

(m) initial: t = 35 (n) optimal: t = 35

(o) initial: t = 40 (p) optimal: t = 40

FIGURE 10. The elastic deformation of structure with time for initial and optimal designs of test case #9. The displacements are magnified by factor 10 for the better illustration. Contours show the distribution of dilatation stress inside the structure.

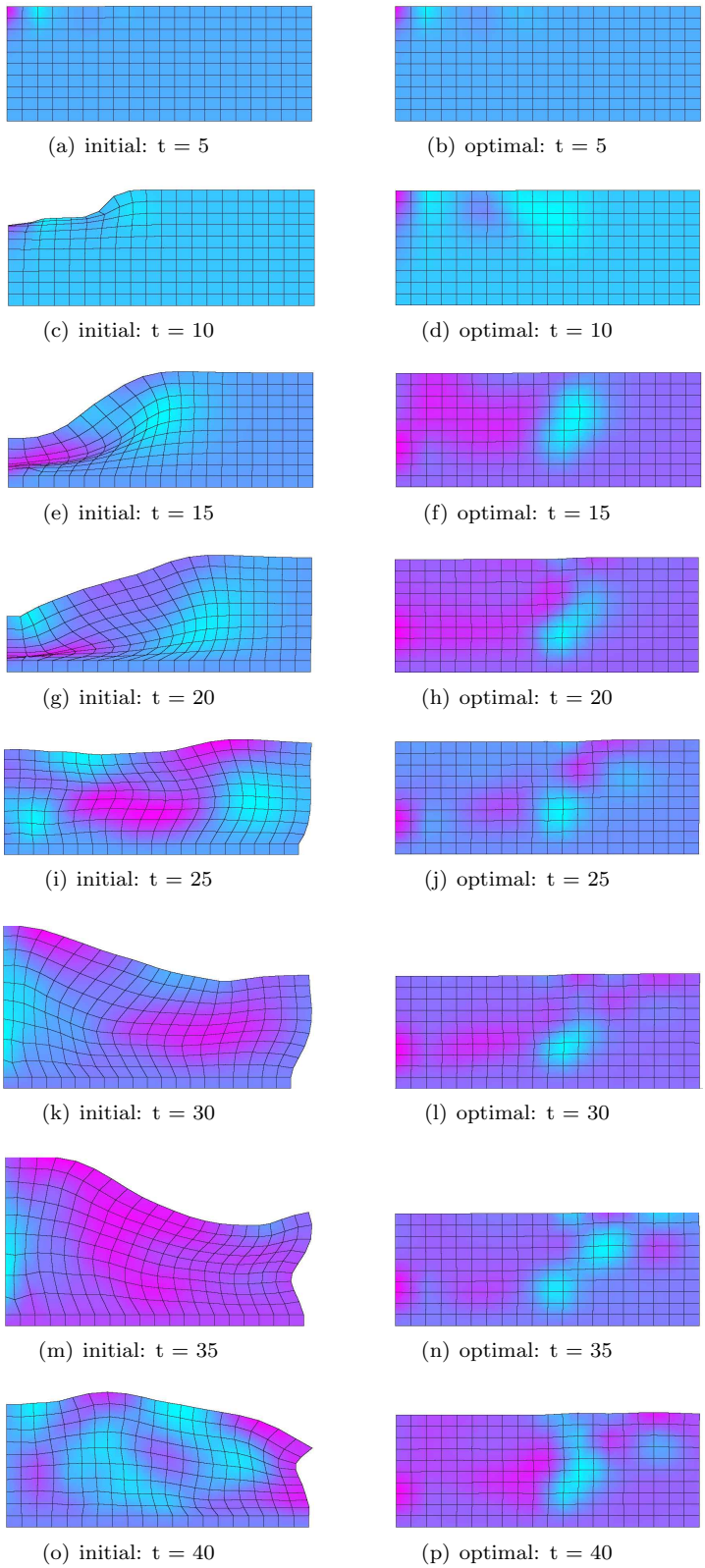

(a) initial: t = 5 (b) optimal: t = 5

(c) initial: t = 10 (d) optimal: t = 10

(e) initial: t = 15 (f) optimal: t = 15

(g) initial: t = 20 (h) optimal: t = 20

(i) initial: t = 25 (j) optimal: t = 25

(k) initial: t = 30 (l) optimal: t = 30

(m) initial: t = 35 (n) optimal: t = 35

(o) initial: t = 40 (p) optimal: t = 40

FIGURE 11. The elastic deformation of structure with time for initial and optimal designs of case #12. The displacements are magnified by factor 10 for the better illustration. Contours show the distribution of dilatation stress inside the structure.